



Ground Movement in the Hanging Wall of Underground Iron Mines with Steeply Dipping Discontinuities: A Case Study

Tianlong Wang^{1,2} · Congxin Chen^{1,2} · Kaizong Xia^{1,2} · Yong Shao^{1,2} · Xuanting Liu^{1,2} · Kuoyu Yang³

Received: 25 May 2022 / Accepted: 1 March 2023 / Published online: 3 May 2023
© King Fahd University of Petroleum & Minerals 2023

Abstract

To ensure the safety of underground mining activities and effectively protect the surface production facilities and houses of the nearby residents, the ground movement caused by the sublevel caving method needs to be studied. In this work, the failure behaviors of the surface and drift of the surrounding rock were investigated based on the results of in situ failure investigations, monitoring data, and engineering geological conditions. The results were then combined with theoretical analysis to reveal the mechanism responsible for the movement of the hanging wall. Driven by the in situ horizontal ground stress, horizontal displacement plays an imperative role in both the movement of the ground surface and underground drifts. Accelerated movement is found to occur in the ground surface which coincides with the occurrence of drift failure. Failure occurs in the deep rock masses and then gradually propagates to the surface. The steeply dipping discontinuities are the main reason for the unique ground movement mechanism in the hanging wall. As steeply dipping joints cut through the rock mass, the rock surrounding the hanging wall can be modeled as cantilever beams subjected to in situ horizontal ground stress and lateral stress due to caved rock. This model can be used to obtain a modified formula for toppling failure. Also, a mechanism of fault slipping was proposed, and the condition required for fault slipping was obtained. Based on the failure mechanism of steeply dipping discontinuities, the ground movement mechanism was proposed considering the horizontal in situ ground stress and caved rock mass: slippage of fault F3, slippage of fault F4, and toppling of rock columns. Based on the unique ground movement mechanism, the goaf surrounding rock mass could be divided into six zones: a caved zone, a failure zone, a toppling-slipping zone, a toppling-deformation zone, a fault-slipping zone, and a movement-deformation zone.

Keywords Underground mining · Hanging wall · Ground movement · Steeply dipping discontinuities

1 Introduction

China has many metal mines distributed across its length and breadth, e.g., the Chengchao Iron Mine, Jinchuan Nickel Mine, and Jinshandian Iron Mine, etc. Many different mining

methods are used to extract the underground metal orebodies, but the one that is most often used is probably sublevel caving. When an orebody is mined, the balanced state of the stress that originally existed in the surrounding rock near the goaf is destroyed. This causes the rock strata to move and deform. Ultimately, this can lead to the failure and large-scale collapse of the drifts and cracking and subsidence on the surface. The deformation therefore has a significant impact on the stability of the drifts and hence the safety of the buildings and structures on the surface. To ensure the safety of the underground mining activities and protect the surface production facilities and residential houses nearby, it is essential that the mechanism responsible for the movement of the ground due to sublevel caving mining should be investigated. To date, numerous scholars, both in China and abroad, have studied ground surface movement in, for example, the Kiirunavaara, Chengchao, and Jinshandian iron mines and Jinchuan Nickel Mine, to name just a few.

✉ Tianlong Wang
tlwang@gzu.edu.cn

✉ Kaizong Xia
kzxia@whrsm.ac.cn

¹ State Key Laboratory of Geomechanics and Geotechnical Engineering, Institute of Rock and Soil Mechanics, Chinese Academy of Sciences, Wuhan 430071, Hubei, People's Republic of China

² University of Chinese Academy of Sciences, Beijing 100049, People's Republic of China

³ School of Civil Engineering and Architecture, Henan University, Kaifeng 475004, Henan, People's Republic of China



Lupo [1] divided the ground surface surrounding the Kiirunavaara Iron Mine into three zones corresponding to: a caved rock zone, a large-scale surface cracking zone, and a continuous surface subsidence zone. Modeling packages (PHASE2 and PFC2D) were used which indicated that the break angle and limit angle remain almost constant as the mining level gets progressively deeper. Apparently, the caved rock and backfill in the pit can provide support to the footwall and hanging wall and thus reduce the subsidence effect (in terms of magnitude and extension) [1]. Time–displacement, time–inverse velocity, and time–velocity curves have also been used to study the different stages of the ground surface deformation encountered [2–6].

The characteristics of the ground surface cracks, ground deformation, movement and collapse mechanisms in the Chengchao Iron Mine have been extensively investigated via in situ field investigations, displacement monitoring, and modeling using Universal Distinct Element Code (UDEC) [7–11]. Li et al. studied surface cracks in the Jinning Phosphate Mine by numerical simulations and physical model experiments [12].

The horizontal displacement of the underground roadway in the Jinchuan Nickel Mine has been found to be larger than the displacement in the vertical direction. In addition, the maximum cumulative vertical displacement in the hanging wall surface is smaller than that in the footwall. Nearly all the plane displacement vectors in the mining area were found to point toward the mined-out area [13, 14]. In their studies on the Jinshandian Iron Mine, Xia K et al. found that the ratio of the horizontal to vertical displacement generally increased the further, one moved away from the boundary of the mined voids, and fault reactivation played an important role in ground movement [15–17]. Other methods, such as differential interferometric synthetic-aperture radar, FLAC3D, and modification of the influence function, were also used to study ground movement and surface collapse in other mines [18–21].

A large body of information has been gathered on the deformation and failure of underground openings, tunnels, and roadways by scholars in China and elsewhere using theoretical, numerical, and field-monitoring approaches. The zone of disturbance around an underground opening can be divided into a failure zone, an open zone, and a shear zone. Hence, many problems relating to the squeezing potential of rocks around tunnels and the stability of practical excavations have been studied [22, 23].

UDEC, 3DEC, and FLAC3D methods have been used to simulate the mechanisms underlying the stability behavior of roadways and progressive failure of roofs [24–27]. Many scholars have found that faults are the main reason for roof collapse. They affect the magnitudes and directions of in situ stresses present, and the dips, locations, and shear strengths of the faults play a significant role in determining the stability

of underground openings [28–32]. Displacement monitoring alone may not be able to provide adequate warning of impending roof fall. However, stress and seismic monitoring can give reliable warning of caving events. The most sensitive factor appears to be the internal friction angle of the intact rock when it comes to the maximum tunnel displacement [33, 34]. Li et al. analyzed the situation surrounding a large underground cavern that had been studied via in situ investigation, conventional measurements, microseismic monitoring, and discrete element modeling [35]. Yang proposed an explanation for why drift failure occurred when an iron orebody was mined out [36].

Scholars tend to study just surface deformation or underground drift damage — they do not combine the information gathered about the underground and surface rock mass deformation. Most of the failure mechanism of surrounding rock is the coal mine goaf. There are few studies covering the failure mechanism of the surrounding rock in the goaf of the metal mine, especially for the failure of the surrounding rock mass with the steeply dipping discontinuities. The rock masses surrounding metal mines have a complex structure. They tend to contain lots of joints, faults and are subjected to horizontal in situ ground stress, and there are often sets of steeply dipping discontinuities that dominate the behavior of the rock mass. After an orebody is mined, the roof of goaf collapses under its own weight and this disturbance gradually spreads to the surface. At the same time, the effect of mining unloading causes horizontal in situ ground stress released, and deformation and destruction of the surrounding rock masses in the mined-out area occur. As the mining activity moves to deeper levels, the scope of the damage continues to extend and a continuous slipping surface is formed which migrates to the surface. This will cause large-scale movement of the surface and horizontal movement may also occur in some regions. Meanwhile, ground movement leads to the destruction of the rock surrounding the goaf, and the drifts are damaged during their service lives. Therefore, it is the steeply dipping discontinuities in the rock masses of metal mines that are the dominant factor causing the large-scale movement of the rock in the mining area.

At present, the mechanism by which ground movement is induced by sublevel caving in metal mines with steeply dipping discontinuities remains unclear. There are few studies evaluating the relationship between the damage caused to the rock surrounding the drifts and deformation of the ground surface due to the movement of the ground in underground mines. As a result, the predicted range of surface movement is far less than that actually found in practice.

This paper takes the eastern area of the Jinshandian Iron Mine as its study subject. One aim is to take into full consideration the complex geological conditions present (steeply dipping discontinuities), and the effects of horizontal in situ ground stress and lateral pressure on the caved rock mass. The

surface and underground monitoring data and field investigation results are combined with a theoretical analysis in order to reveal the mechanism by which the steeply dipping discontinuities affect ground movement. The results of our study should provide a useful reference for future orebody mining in similar iron mines.

2 Details of the Mining Site

The Jinshandian Iron Mine is located in Jinshandian town, which is 30 km southwest of Huangshi City, Hubei Province, China. It is a large-scale underground metal mine with an approximate area of 3.5 km² and an annual output of 3 million tons. Sublevel caving is used to extract the ore. The eastern mining area of interest lies between exploratory lines 25 and 43 (Fig. 1). There are lots of residential villages, railways, stations, and other buildings and structures on the surface in this region. Steeply dipping discontinuities are common in the mining area, and there are four east–west-directed faults distributed from north to south (labeled F1–F4 in Fig. 1).

2.1 Lithology

The most widely distributed lithologies in the eastern area of the Jinshandian Iron Mine are hornstones, marbles, magmatic rocks (mainly quartz diorite), and the orebodies. The quaternary overburden on the surface has a thickness ranging from 0 to 20 m. The hanging wall is widely distributed with hornstone, the specific distribution of which is shown in Fig. 1.

Two boreholes (CK1 and CK2) were drilled to a depth of about 160 m in the hanging wall to reveal the underground lithology (Figs. 1a and b). The boreholes CK1 and CK2 are about 400 and 200 m away from the mined-out area, respectively. The core sample from CK1 mainly reveals the presence of argillaceous hornstone. There is also a layer (about 10 m thick) of palimpsest siltstone at the bottom of the borehole. Joints and fissures are common and form an irregular network. The fissure surfaces are mostly filled with quartz or mud, and the average rock quality designation of the entire borehole is 55.65%. The CK2 core sample alternates between palimpsest siltstone and argillite hornstone, and joints and fractures occur throughout them. The borehole collapsed many times during drilling, leading to a broken rock core sample with an average rock quality designation across the whole borehole of 39.36%. Thus, it appears that the closer one is to the goaf, the poorer the quality of the rock mass and the more prevalent the presence of weak fracture zones.

2.2 Discontinuities and faults

2.2.1 Discontinuities

Geological surveys were carried out on the rock masses on the surface, as well as the rocks surrounding the drifts of the – 340, – 354, – 368, – 382, and – 396 m levels.

The discontinuities in the hanging wall were then classified and summarized, as shown in Fig. 1c. There are three main groups of dominant discontinuities in the hornstone (Table 1).

2.2.2 Faults

The mining area is crossed by four parallel fault zones with east–west strikes in plane projection (F1–F4 in Fig. 1). This paper is mainly concerned with faults F3 and F4 as they have the most impact on the hanging wall.

Fault F3 lies between exploratory lines 25 and 43. It dips to the south and has a dip angle that ranges from 55 to 87°. The southern part of the fault rises and moves eastwards, while the northern part descends and moves westwards. The fracture zone of the rock mass in the fault lies in the range from 15 to 35 m.

Fault F4 runs throughout the entire region (shown in Fig. 1d). It is roughly parallel to F3 and lies 25–150 m to the south of it. It also dips to the south and has a dip angle in the range from 55 to 85°. The southern part of the fault rises and moves eastwards, while the northern part descends and moves westwards. The fracture zone of the rock mass in the fault is generally 10–35 m wide.

F3 and F4 coalesce near exploratory line 42, forming a 100-m wide fault zone on the surface.

2.3 In situ ground stress

Ge et al. [37] collected a large amount of data on the in situ ground stress near the Jinshandian Iron Mine area. In 1986, the in situ stress was measured in the Liujiawan mining area of the Lingxiang Iron Mine and the direction of the maximum principal stress was found to be NE15–34°. Principal stresses of 6.82 and 5.37 MPa were measured at two monitoring points in the Tonglushan Mine (located in the marble at a depth of about 180 m below the surface) and the gravitational stress was found to be 4.86 MPa. According to the study by Ge et al. [37] the maximum principal stress on the rock in the Jinshandian Iron Mine lies in the north–south direction (N10°E) and the medium principal stress lies in the east–west direction (N80°W).

In 2019, the stress relief method was used to obtain the in situ ground stresses in Jinshandian Iron Mine, $\sigma_1 = 1.47\gamma h$ and $\sigma_2 = 1.30\gamma h$, where γh is the self-weight stress, with the

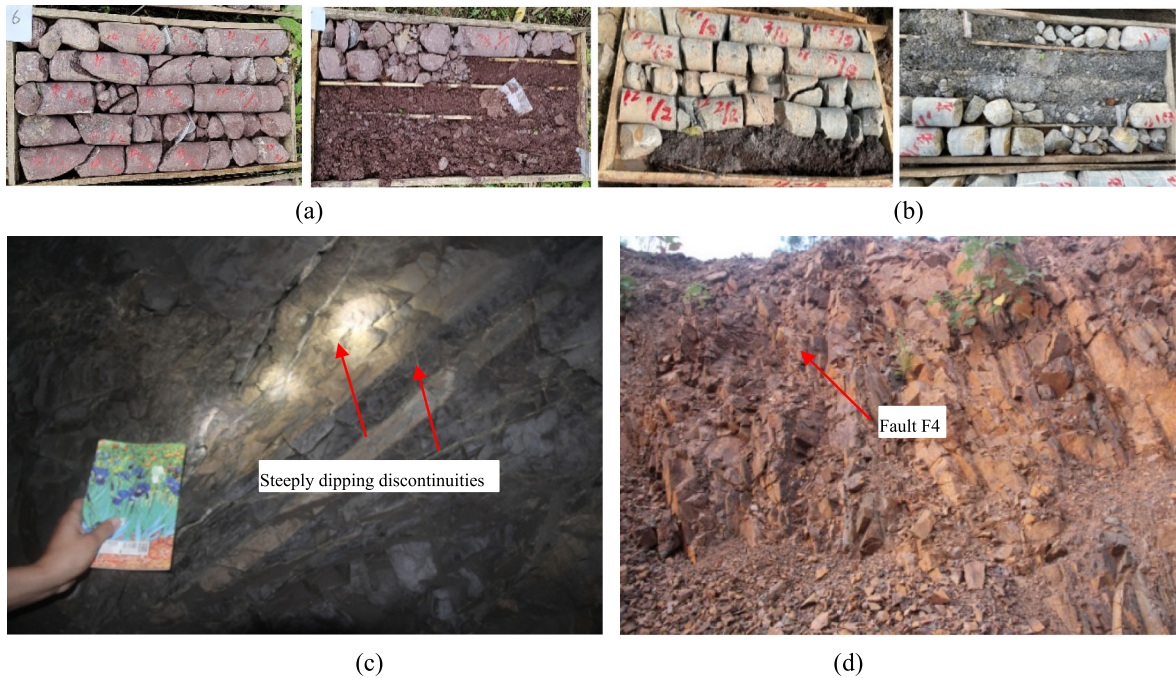
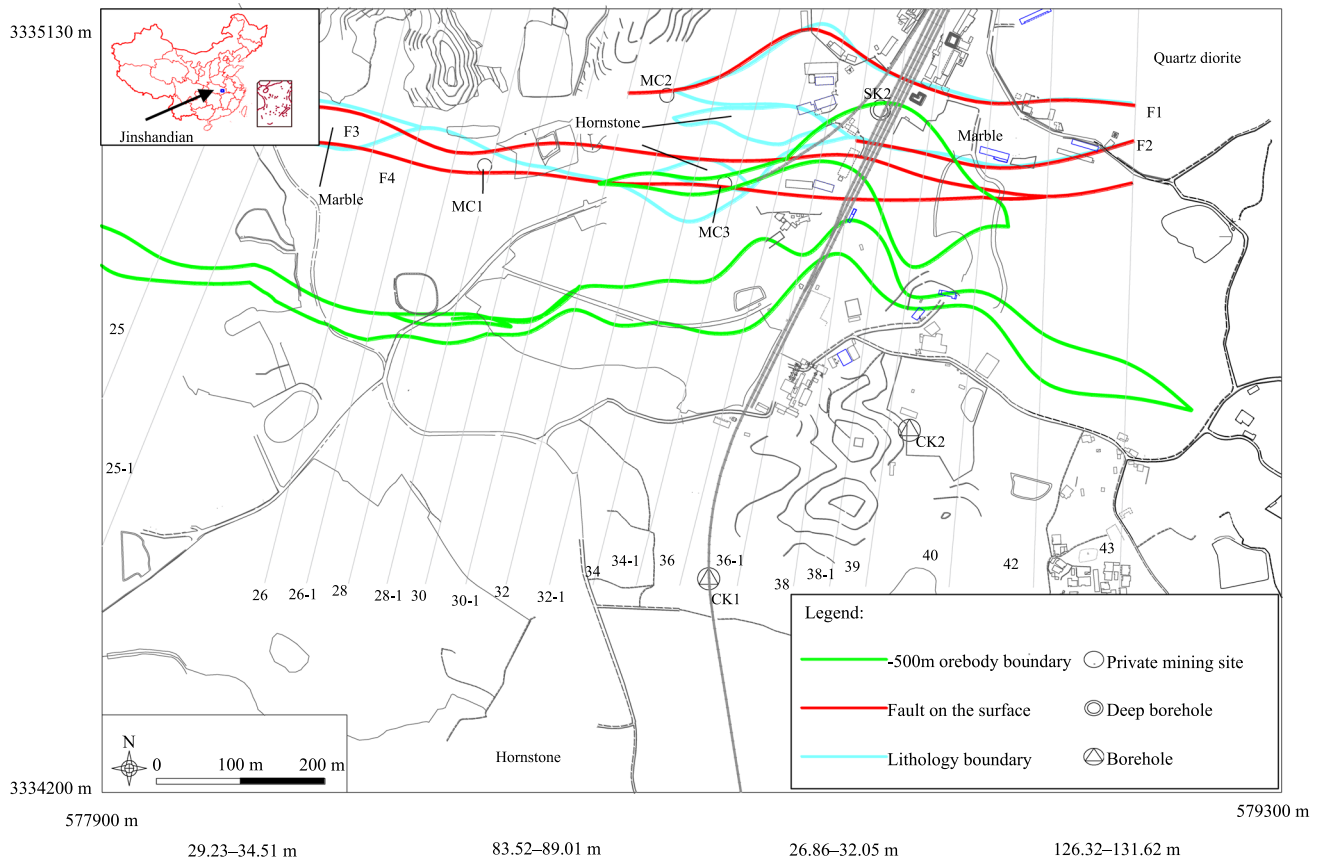


Fig. 1 Lithology, faults, joints, orebodies, boreholes, deep boreholes, and private mining sites in the study area. **a** and **b** CK1 and CK2 core samples from the boreholes, **c** discontinuity in the – 354 m sublevel

drift (near the 714 wind shaft), **d** discontinuity visible on the ground surface (fault F4 near the collapse pit no. VI)

Table 1 Discontinuities in the hanging wall

Number	Attitude of the major discontinuity surface in the hanging wall			
	Dip direction	Strike	Dip angle (°)	Spacing (m)
1	S37°W	S53°E	70	0.5
2	S76°E	S14°W	78	–
3	S1°W	S89°E	66	0.30

maximum principal stress approximately lying in the direction N15°E.

2.4 Description of the Orebodies

2.4.1 Orebody Distribution

The eastern area of the Jinshandian Iron Mine contains two main ferrous orebodies: Fe I and Fe II. Fe II lies to the north of Fe I by 15–200 m and they are imbricated and parallel when viewed in cross section. The orebody Fe I is about 20–80 m thick and occurs at an elevation of + 16 m to – 1,000 m; it has a relatively simple and regular shape. Fe II occurs at an elevation of + 70 m to – 719 m. This orebody is exposed to the surface between the 26 and 34 exploratory lines. Its shape is more complicated than that of Fe I and it is 10–150 m thick.

2.4.2 Mining Method

The Jinshandian eastern area was mined using the sublevel caving method. The stopes were arranged in the vertical direction of the orebody. The length of a stope was equal to the thickness of the orebody, and its width was 16 m. The level height was 70 m and the sublevel height was 14 m so that each level is divided into five sublevels. Below the – 410 m level, a different scheme was used in which the level height was 90 m and six sublevels were formed. (The height of each sublevel was 15 m.).

2.4.3 Mining Situation

In September 2005, the roof of the – 270 m level began to cave. Orebody Fe I was mined from north to south, while orebody Fe II was mined from south to north. Due to relocation problems on the ground surface, mining work had to be suspended from early April 2009 to the end of February 2012. Mining resumed in early March 2012. Due to the COVID-19 pandemic, mining work had to be stopped on January 18, 2020; it subsequently resumed in March 21, 2020. Table 2 displays more details of the mining regime employed.

Mining is currently taking place in the – 382 and – 396 m levels. A pictorial representation of a part of this situation with respect to mined-out areas is shown in Fig. 2.

Table 2 Mining regime employed

Mining level (m)	Mining dates	
	Start	End
– 270	Feb 2007	Apr 2009
– 284	Dec 2007	Dec 2012
– 298	Mar 2012 Fe I and Fe II	Sep 2013 Fe I and Jun 2014 Fe II
– 312	Apr 2012 Fe II and Dec 2012 Fe I	Jun 2014 Fe I and Nov 2014 Fe II
– 326	May 2014 Fe I and Dec 2014 Fe II	Aug 2015 Fe I and Mar 2016 Fe II
– 340	Mar 2015 Fe I and Fe II	Mar 2016 Fe I and Apr 2017 Fe II
– 354 ^a	Dec 2015 Fe I and Feb 2017 Fe II	Apr 2017 Fe I and Apr 2018 Fe II
– 368 ^b	Feb 2017 Fe I and Feb 2018 Fe II	Oct 2019 Fe II and Dec 2018 Fe I
– 382 ^c	Feb 2018 Fe I and Aug 2018 Fe II	Nov 2020 Fe II and Fe I
– 396	Mar 2019 Fe I and Jun 2019 Fe II	Mining

^aFe I was mostly mined in April 2017, the orebody east of exploratory line 39 was mined in December 2018

^bFe I was mostly mined in December 2018, the orebody east of exploratory line 39 was mined in July 2020

^cFe I was mostly mined in November 2020, the orebody east of exploratory line 39 is currently being mined

In addition, as the orebodies were directly exposed on the ground surface in certain places, many private mining sites had been put into operation. The three main private mining sites were marked MC1, MC2, and MC3 in Fig. 1. It is understood that the mining depth in these private mines was about – 160 m and the total amount of stoping ore was about 2 million tons.

3 Ground Surface Collapse and Cracking

The scopes of the surface collapse and cracking, and damage caused to buildings and structures, were investigated based on data derived from field investigations, three-dimensional (3D) laser scans, and drone photography. The results (to December 2020) are summarized in Fig. 2.

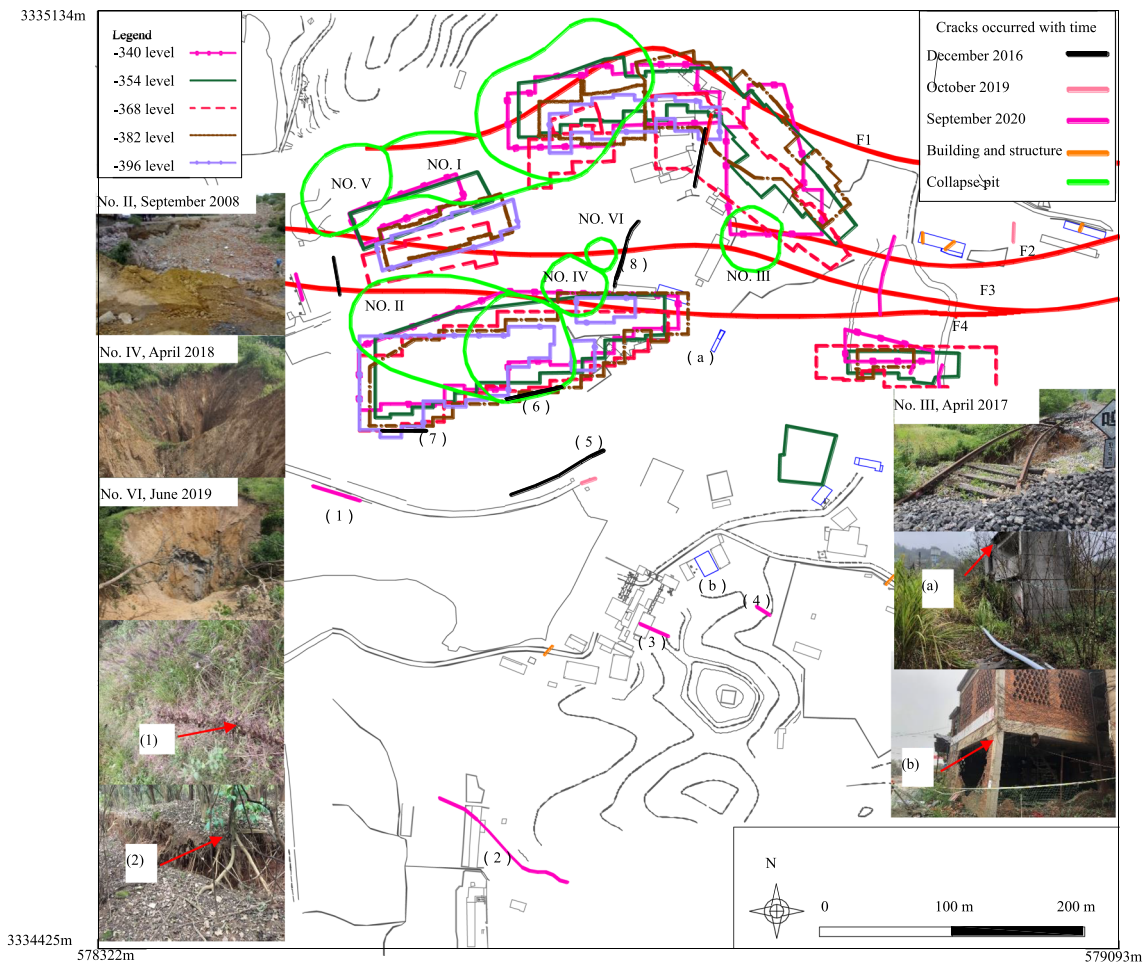


Fig. 2 Planar projection of the collapse pits and cracks

In September 2008, the surface of the hanging wall began to collapse near MC3 (forming collapse pit no. II). Its extension was small until production was suspended in February 2012 and after March 2012 it slowly extended outwards. In November 2013, a new collapse pit with an area of about 300 m² appeared on the ground next to collapse pit no. II and two collapse pits finally merged into one large collapse pit. From April 2017 to June 2019, three collapse pits (nos. III, IV, and VI) sequentially appeared in the hanging wall and the depths and widths of the pits continued to increase. The appearance times, locations, and sizes of the collapse pits are shown in Table 3.

A large number of cracks have appeared on the surface in the hanging wall and have continued to extend away from the goaf (see Fig. 2). Before 2016, there were more cracks in the footwall than the hanging wall. After December 2016, the cracks in the hanging wall gradually began to increase (cracks 5–8). Crack 1 was found in September 2020 and was roughly 120 m away from collapse pit no. II. Crack 2 was about 340 m away from collapse pit no. II and had a maximum

width of 40 cm. The strikes of cracks 1–4 were the same as that of the S53°E discontinuity (Table 1, first group). The cracks in the hanging wall had tensile properties, which was caused by ground movement of rock mass.

Signs of damage were also found in the buildings around the collapse pits. The brick building labeled ‘a’ in Fig. 2 was about 45 m away from collapse pit no. III. It was found that its northeastern side (collapse pit no. III side) had sunk into the ground by a considerable amount. The beam-column of building ‘b’ was about 172 m away from collapse pit no. II — its column was found to clearly lean toward this pit.

Collapse pit no. II, which appeared in September 2008, was located above Fe I. It was originally formed due to the private mining activity taking place in MC3 and not due to the broken rock mass formed by the underground goaf at that time. However, as the mining activity continued to deeper levels, the range of damage experienced by the deep rock masses began to extend upwards. In December 2016, collapse pit no. II became larger and deeper, resulting in large deformation of the ground surface. In April 2018, collapse

Table 3 Surface collapse pits in the hanging wall

Pit number	Time of appearance	Location	Area, width, and depth
I	April 2007	Near mining site MC2	250 m ²
II	September 2008	Near mining site MC3	620 m ²
III	April 2017	Near exploratory lines 38/38-1	Diameter 6 m; depth 3 m
IV	April 2018	Near exploratory lines 34-1 to 36	Diameter 20 m
V	November 2018	Near exploratory lines 30-1 to 32	Diameter 18 m; depth 10 m
VI	June 2019	East of collapse pit IV	Diameter 5 m; depth 5 m

Surface collapse occurred again in the vicinity of collapse pit nos. II and I in February and May 2013, respectively. A new pit appeared in collapse pit no. II on June 2019

pit no. IV emerged, which was located near the collapse pit no. II. In June 2019, a new collapse pit, no. VI, appeared near pit no. IV and a new collapse pit appeared inside collapse pit no. II. At this time, collapse pits II, IV, and VI formed a large group of collapse pits. In effect, by December 2016, the caving of the deep rock mass had spread to the ground surface forming a large-scale area of deformation above the mined-out area. It should be pointed out that collapse pits no. IV and VI were located between fault F4 and fault F3, and the two collapse pits were not directly above the ore body. Due to the slippage of the fault caused by underground mining, the rock mass around the fault moves down together with fault. This is the main reason for the emergence of collapse pits IV and VI.

According to the investigation of surface collapse and cracking, it can be found that ground surface collapse, surface cracks, and building cracks are related to the steeply dipping discontinuities. In the early stage of mining, tensile cracks (along the weak joints strike) first appeared on the surface. As the mining deepened, a collapse pit began to appear on the surface, and the surface deformation continued to extend outwards, causing cracking and destruction on buildings and structures. The slippage of the fault accelerated the destruction of the roof of goaf, and a large amount of rock fell into the goaf, causing the surface to collapse. The rock mass around the goaf began to move toward the goaf. More cracks and collapses then occurred, and the buildings and structures began to crack and fail, some tilting toward the goaf.

4 Characteristics of the Drift Failure

The deformation of the underground drifts and surrounding rock was investigated via field surveys and microseismic monitoring. The characteristics of the damage to the drift, scope of the drift failure, and rupturing of the surrounding rock were thus determined.

4.1 Field Investigation

The field investigation implied that the hanging wall has suffered damage that is more serious than that in the footwall. For example, the haulage drifts in the – 340 and – 410 m levels began to show obvious signs of failure in October 2016 and January 2017, respectively. In March 2017, July 2018, and December 2018, failure was also observed in the haulage drifts of the – 354, – 368, and – 382 m sublevels, respectively.

The failure of the drifts in the – 340 to – 410 m levels was investigated from March 2018 to May 2019 (Fig. 3). In the – 340 m level, drift failure was mainly encountered between the 34 and 39 exploratory lines, wherein the main form of damage was the collapse of the roof of the haulage drift. The state of the sublevel drifts was not investigated due to the severity of this damage.

The haulage and production drifts in the – 354 m sublevel suffered severe damage between the 34 and 38 exploratory lines (Fig. 3b). The damage was mainly in the form of large-scale continuous collapse, the main characteristics being spalling at the bottoms of the drifts and collapse of the roofs.

The failure in the drift in the – 368 m level was mainly observed between exploratory lines 34 and 38 and 39 and 40 (Fig. 3c). This mainly involved sidewall failure and roof fall in certain places. Toppling failure also occurred in the sublevel haulage drift far away from the goaf side between the 18 and 19 production drifts. The sublevel haulage drift between the 15 and 16 production drifts was also deflected to the side of the goaf. In the – 382 m level, sidewall failure occurred in the sublevel haulage drift between exploratory lines 34 and 36.

In the – 410 m level (Fig. 3d), drift failure was found to occur between exploratory lines 36 and 38. This mainly consisted of sinking and cracking of the roof. Circumferential fractures appeared in the roof where the axis of the 712 transverse drift was perpendicular to the strike of the fault. In places where the axis of the 712 transverse drift made a 45° angle with the strike of the fault, vertical fractures appeared in the sidewall.

The sublevel haulage drifts in the hanging wall mainly failed near the mined-out areas. As the distance from the mined-out areas increased, the severity of the failure gradually decreased. Moving along the strike of the orebody from west to east, the damage incurred by the surrounding rock



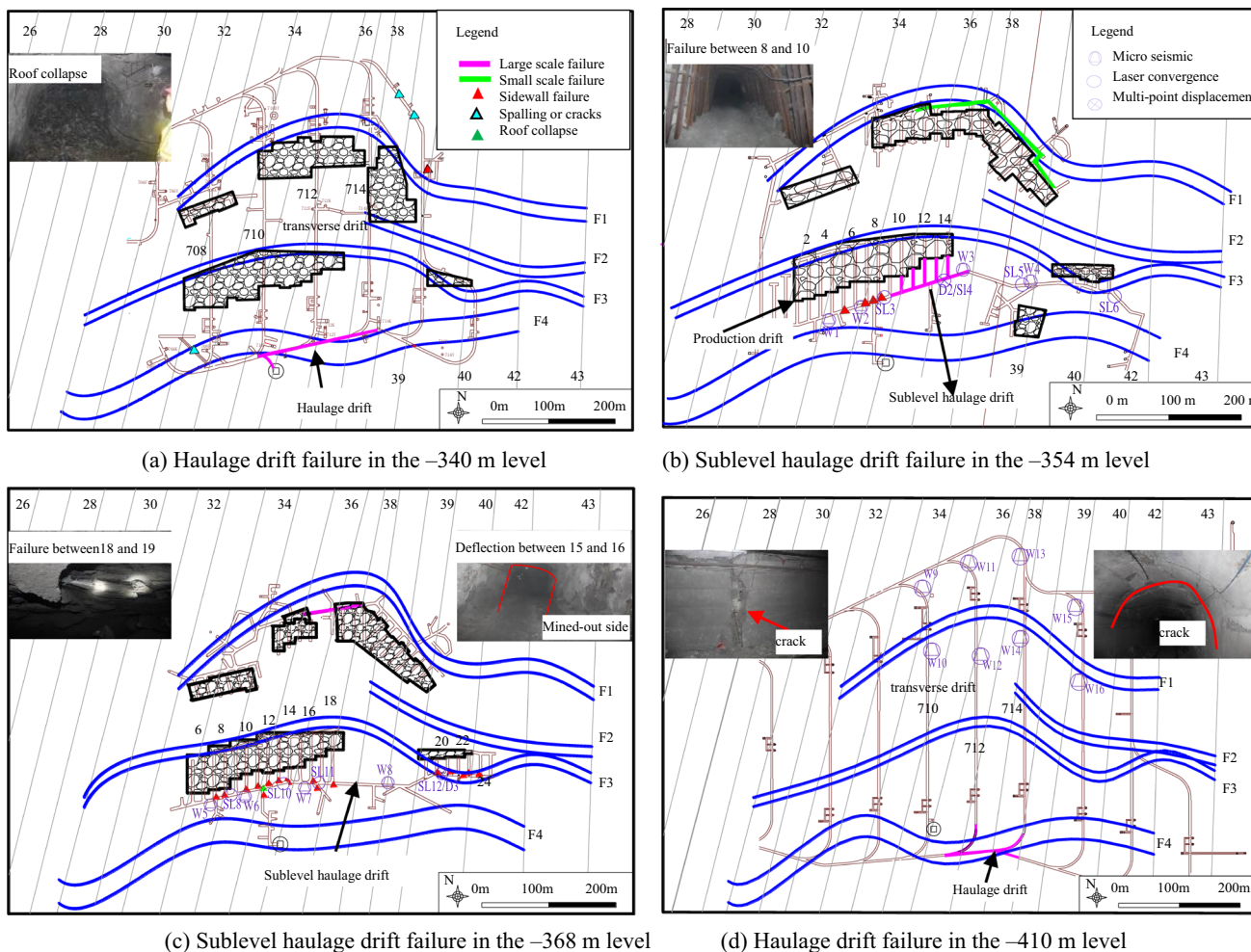


Fig. 3 Characteristics and range of the failure in the drifts

gradually increased. The range of the damage to the surrounding rock in the hanging wall was also becoming larger than that found in the footwall. The damage was less severe with increasing depth (e.g., the damage in the sublevel haulage drifts in the - 410 m level was less than that in the haulage drifts in the - 340 m level). The haulage drifts in the - 340 m and - 410 m levels were located inside the fracture zone of fault F4. When mining was carried out, the roofs of these drifts would therefore find it difficult to bear the loads they experience. If they became unstable, then slippage would occur and the drift would undergo failure. Furthermore, the most serious failure occurred in the - 340 m level.

The roof of goaf, sublevel and level haulage drifts were affected by the steeply dipping faults F3, joints and fault F4, respectively. After the orebody was mined, F3 slipped due to the mining disturbance which caused the roof of the goaf to fail and increased the goaf space. Under the action of the horizontal in situ ground stress, the anti-dipping rock columns formed by the steeply dipping discontinuities that

cut through the rock mass also began to topple and did so toward the goaf. Damage was thus caused to the sublevel haulage drifts between - 340 m and - 382 m. With the deepening of mining, the damaged rock mass would form a slipping surface, which was continuously propagated to the ground surface. By connecting the boundary of the surrounding rock between the - 368 m level and the -382 m level drift, it is estimated that the line and the horizontal plane had an angle of about 60° between them. The mining activity and occurrence of rock mass toppling failure induced fault F4 to slip. This led to the failure (roof collapse, cracking, etc.) of the haulage drifts between the - 340 m and - 410 m levels.

4.2 Microseismic Monitoring Experiments

A series of horizontal holes were drilled in order to carry out microseismic monitoring experiments. A drill bit of diameter 80 mm was used, and the holes were drilled to a depth of about 5 m. Microseismic sensors were subsequently placed in the

holes, the locations of which are shown in Figs. 3b–d. (In the hanging wall region, they were arranged in the sidewalls of the sublevel haulage drifts in the – 354 m and – 368 m levels; in the footwall, they were located in the transverse drift in the – 410 m level. The distance between two adjacent sensors was about 80 m.)

A large amount of microseismic data could be recorded during the 8-month-long monitoring period (from December 2018 to July 2019). The results of these experiments are shown in Fig. 4.

Figure 4a indicates that many microseismic events occurred in the hanging wall during the monitoring period and that these events were mainly concentrated near the mined-out areas. This suggests that the quality of the rock in the footwall was much better than that of the rock in the hanging wall. The quality of the surrounding rock in the hanging wall was clearly significantly affected by the nearby mining activity. The micro-fracturing that occurred in the hanging wall was clearly concentrated in the region between faults F3 and F4 (Fig. 4a) and between the – 340 m and – 410 m levels (Fig. 4c). Because of this, it is interesting to examine the distribution of the microseismic events that occurred along exploratory line 36 in more detail.

Figure 4b shows the spatial distributions of the events occurring along line 36 in two months in 2019 displayed as vertical profiles. By the beginning of January 2019, only a small part of the orebody in the – 382 m level had been mined near exploratory line 36. (Most of it was mined in June 2019.) It shows that a large number of microseismic events were generated as the orebody in the – 382 m level was mined in January 2019. Moreover, these events occurred both below and above the mining level. The microseismic events also appeared to be linearly distributed along a line that was inclined at an angle of about 60° to the horizontal. This was because a large number of micro-fractures were formed as toppling failure occurred along the steeply dipping discontinuities in the rock mass. As mining continued, the number of microseismic events between faults F4 and F3 gradually increased. This suggests that the mining activity caused the faults to slip and the slip surface thereby extending into fault F4.

In summary, the mining activity caused fault F3 to slip which caused damage to the roof of the goaf. The anti-dipping rock columns formed by the steeply dipping discontinuities toppled to the side of the mined-out area. The failing rock columns formed a slipping surface inclined at an angle of about 60° to the horizontal. This surface passed through fault F4, inducing it to slip. This led to cracks forming in the haulage drifts and roof collapsing.

5 Characteristics of the Ground Movement

5.1 Displacement Monitoring

Global positioning systems (GPSs) can be used to monitor the horizontal and vertical displacement of the ground surface. Deep boreholes and suitable sensors can be adopted to monitor the deformation of the deep rock masses. Multi-point displacement meters and laser convergence meters can also be arranged within drifts to monitor the horizontal deformation and cross-sectional convergence deformation of the surrounding rocks.

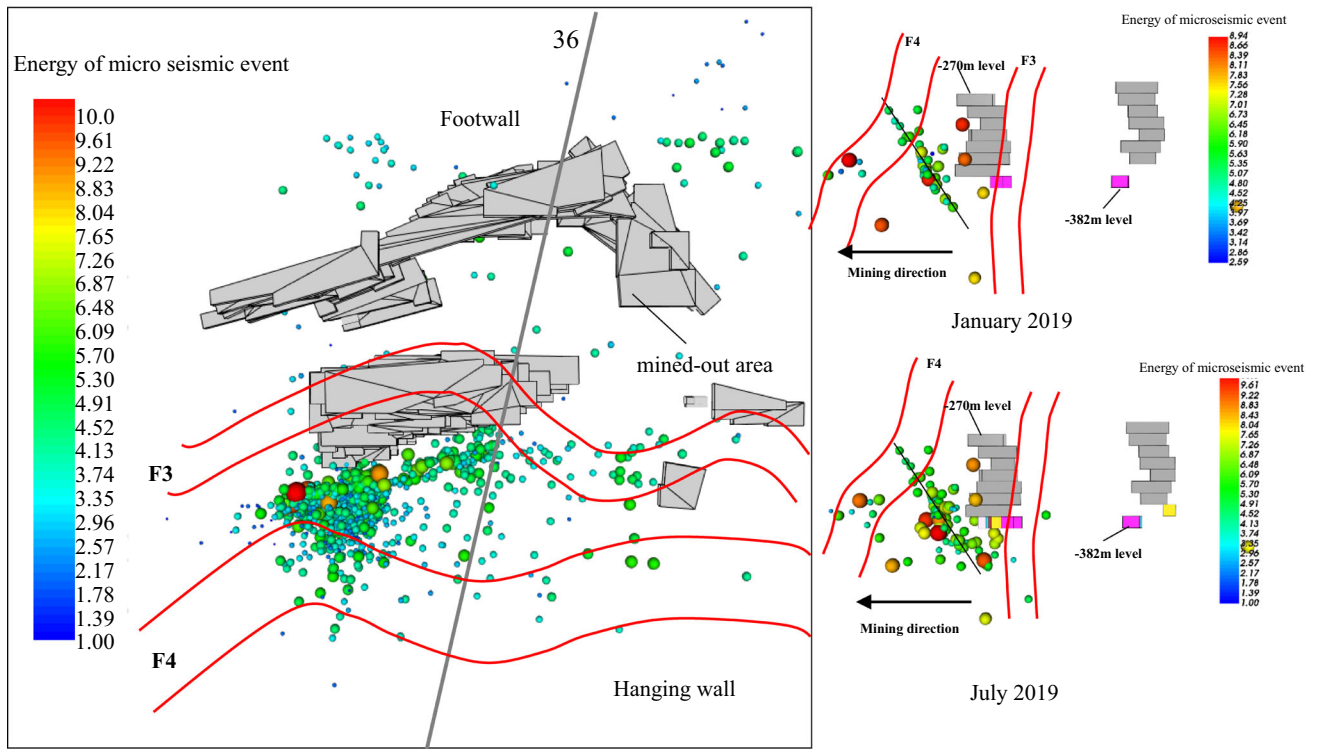
The GPS monitoring network established in the region consists of two parts: two GPS systems with known coordinates that are far away from the mining area and act as fixed reference points (referred to a G1 and G2), and multiple GPS systems at various monitoring points located within the mining area that move with the ground surface. The coordinates of these monitoring points can be derived using two the reference points. The 3D coordinates of the two reference points G1 and G2 are (3,335,533.049 m, 578,779.2745 m, 110.59958 m) and (3,335,331.055 m, 579,266.8118 m, 47.42427 m), respectively. The horizontal and vertical deformation of the ground surface in response to mining can thus be derived using the GPS data recorded.

The movement of the rock mass was more readily investigated via an ultra-deep vertical borehole located in the hanging wall (Xia et al., 2018). Displacement meters were arranged at multiple monitoring points in the borehole at known initial depths relative to the ground surface. (In this work, the monitoring points are initially 45, 93, 141, 189, 240, and 288 m below the surface.) The displacement meters could thus be used to directly observe the vertical displacement of the deep rock mass in the hanging wall relative to the surface.

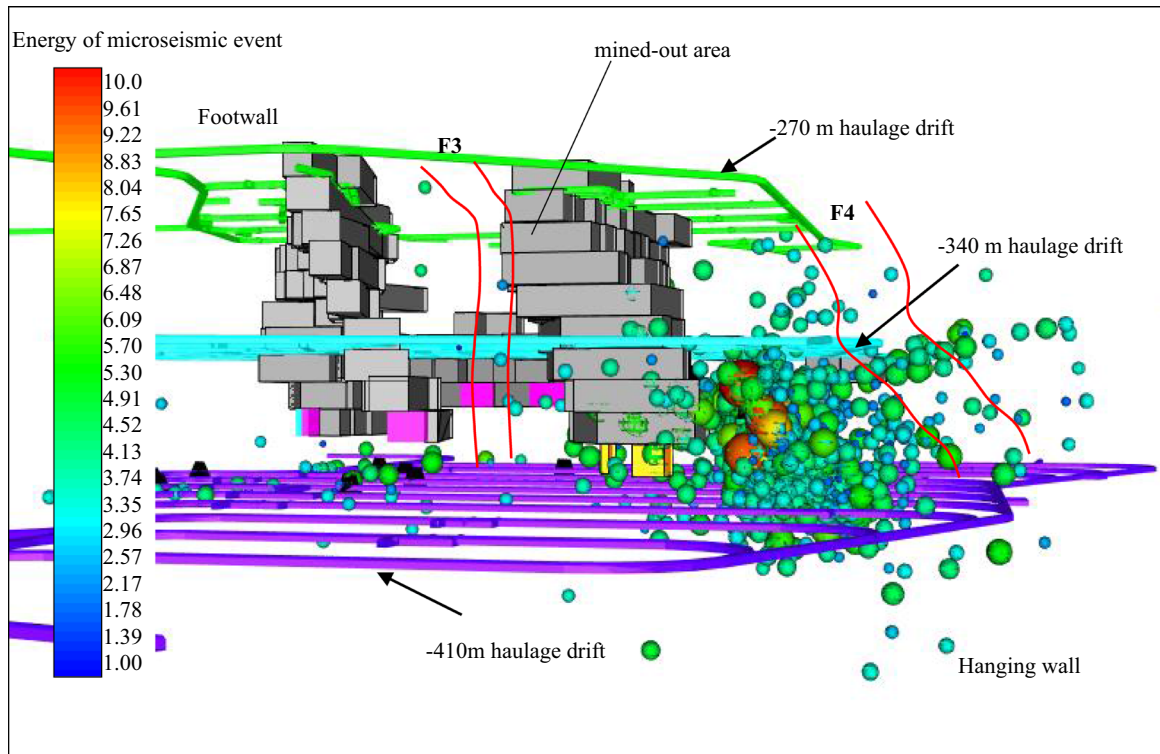
The deformation of the surface of a drift could be monitored using laser convergence meters which are accurate to 1 mm. The convergence meters were fixed to the sidewalls of the drift and aligned. They were then used to monitor the positions of points on the opposite sides of the drift. In this work, six distances were monitored corresponding to the lines 1 to 6 shown in Fig. 7a.

The horizontal displacement of the rock surrounding a drift in the hanging wall could be similarly monitored using multiple displacement meters distributed inside a horizontal borehole. In this work, the boreholes employed have depths of 18 m and the meters used have a measurement accuracy of 0.02 mm. Each monitoring hole hosts 6 equispaced monitoring points labeled P1 to P6 in the order shown in Fig. 8a (i.e., P6 is the closest monitoring point to the drift).





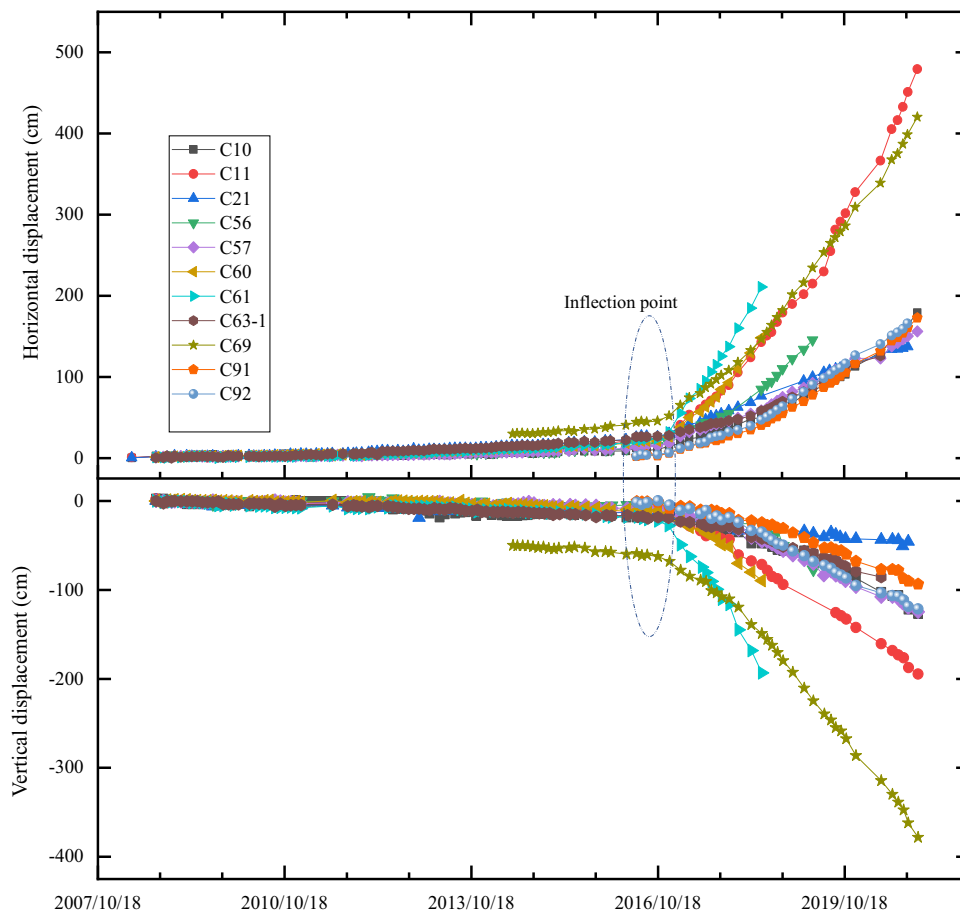
(a) Distribution of the microseismic events in the mined-out area (top view) (b) Distribution of the microseismic events along 36



(c) Distribution of the microseismic events in the mined-out areas (viewed from west to east)

Fig. 4 Distribution of the microseismic events

Fig. 5 Horizontal and vertical displacement curves



5.2 Deformation Characteristics of the Ground Surface

The GPS data recorded at 11 monitoring points in the hanging wall were used to determine the horizontal and vertical positions of the points as a function of time. The corresponding displacement–time curves are demonstrated in Fig. 5.

As can be seen from Fig. 5, the displacements of the monitoring points were initially quite small. As time progressed, their values fluctuated but generally increased only very slowly overall. However, the slopes of the curves suddenly became much steeper sometime after October 2016. That is, the displacements of the points began to change much more rapidly around December 2016, implying that the points were moving much more quickly.

The largest horizontal displacement as shown in Fig. 5, 479.5 cm, was recorded at monitoring point C11. (The locations of the monitoring points were highlighted later on in this script in Fig. 9a.) The largest vertical displacement, however, was recorded at point C69 and amounted to – 378.3 cm. Table 4 indicates that the cumulative horizontal and vertical displacements were very small over the period from May 5, 2008, to October 18, 2016 (as were the corresponding velocities of the monitoring points). After October 2016, however,

the displacements and velocities increased sharply. In fact, the vast majority of the displacement experienced at each monitoring point was generated after October 2016. It is also worth noting that, in general, the closer the monitoring point is to the collapse pit, the larger the displacement experienced. Also, the horizontal displacement of the monitoring points is generally larger than their vertical displacement.

Figure 6 shows the vertical displacements measured in the ultra-deep borehole. As can be seen, the vertical displacement at each depth in the ultra-deep borehole started to increase sharply around October 2016. The largest displacement shown was – 30.6 cm and occurred at a depth of – 288 m. From December 2011 to October 2016, the displacement values only amounted to – 0.18 cm to – 1.16 cm. From October 2016 to April 2017, the displacement value increased rapidly, reaching values between – 12.1 cm (depth equal to – 189 m) and – 30.6 cm (depth equal to – 288 m). This level of displacement was about 30 times the previous cumulative displacement. In the end, the measurements had to be discontinued as the borehole had become severely damaged because of the movement and deformation of the rock mass.

The above results are highly consistent timewise. That is, inflection points occurred in both the ground displacement

Table 4 Cumulative horizontal, vertical displacement and average velocity

Monitoring point	Period	Cumulative displacement (cm)				Average velocity (mm/day)		Ratio <i>H/V</i>
		<i>H_N</i>	<i>H_E</i>	<i>V</i>	<i>H</i>	<i>V_V</i>	<i>V_H</i>	
C10	2008/5/5 to 2016/10/18	10.52	− 2.77	− 16.11	10.88	− 0.05	0.04	0.68
	2016/10/18 to 2020/12/22	155.78	− 89.31	− 110.75	179.56	− 0.73	1.18	1.62
C11	2008/5/5 to 2016/10/18	23.22	− 2.97	− 14.93	23.40	− 0.05	0.08	1.57
	2016/10/18 to 2020/12/22	456.19	12.30	− 148.04	456.36	− 0.97	2.99	3.08
C21	2008/5/5 to 2016/10/18	26.22	0.24	− 14.46	26.22	− 0.05	0.08	1.81
	2016/10/18 to 2020/12/22	91.59	30.16	− 31.30	96.42	− 0.21	0.63	3.08
C56	2008/5/5 to 2016/10/18	9.43	− 14.04	− 5.14	16.91	− 0.02	0.05	3.29
	2016/10/18 to 2019/4/17	45.04	− 90.02	− 71.76	100.66	− 0.79	1.10	1.40
C57	2008/5/5 to 2016/10/18	3.12	− 15.17	− 6.93	15.49	− 0.02	0.05	2.24
	2016/10/18 to 2020/12/22	55.41	− 129.77	− 117.87	141.10	− 0.77	0.92	1.20
C60	2008/5/5 to 2016/10/18	19.71	− 8.21	− 10.91	21.35	− 0.04	0.07	1.96
	2016/10/18 to 2018/6/19	130.82	− 6.27	− 78.69	130.97	− 1.29	2.15	1.66
C61	2008/5/5 to 2016/10/18	10.41	− 21.17	− 22.51	23.59	− 0.07	0.08	1.05
	2016/10/18 to 2018/6/19	82.49	− 168.09	− 170.74	187.24	− 2.80	3.07	1.10
C63-1	2008/5/5 to 2016/10/18	26.68	− 0.76	− 18.31	26.69	− 0.06	0.09	1.46
	2016/10/18 to 2020/5/19	97.86	34.90	− 24.03	103.90	− 0.18	0.79	4.32
C69	2014/6/15 to 2016/10/18	45.97	− 0.27	− 62.51	45.97	− 0.73	0.54	0.74
	2016/10/18 to 2020/5/19	374.05	18.28	− 315.74	374.50	− 2.07	2.45	1.19
C91	2016/6/15 to 2016/10/18	2.89	− 0.64	− 1.42	2.96	− 0.11	0.24	2.09
	2016/10/18 to 2020/5/19	169.82	− 2.72	− 92.06	169.84	− 0.60	1.11	1.84
C92	2016/6/15 to 2016/10/18	4.28	− 1.04	0.07	4.40	0.01	0.35	64.76
	2016/10/18 to 2020/5/19	170.01	29.27	− 121.44	172.51	− 0.80	1.13	1.42

H_N and H_E refer to the cumulative displacement in the north and east directions, respectively; H and V refer to the cumulative displacement in the horizontal and vertical directions, respectively; $H = \sqrt{H_N^2 + H_E^2}$, magnitude of horizontal displacement. V_V and V_H refer to the average horizontal and vertical velocity

data and deep borehole data at around the same time that the rock surrounding the roadway began to show signs of failure, i.e., October 2016. Because of the steeply dipping joints and fault cutting, the rock masses toppled toward the mined-out area and formed a slipping surface. As the underground mining activity moved to deeper levels, the damage to the rock surrounding the drifts continued to propagate to the ground surface. Due to the excessive deformation experienced by the rock mass, the measurements in the ultra-deep borehole could not be continued. Also, the horizontal and vertical displacements of the surface increased sharply after October 2016. Combined with the investigation of surface cracks and collapse, it can be concluded that in December 2016, the underground failure had been propagated to the ground surface. This also explains why the deformation on the surface of the hanging wall mainly occurred after December 2016. In the mining area, the stress in the rock was dominated by the horizontal in situ ground stress. The stress released due

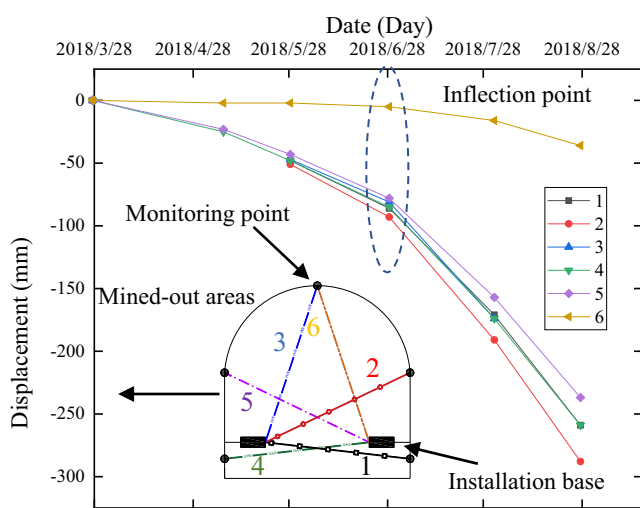
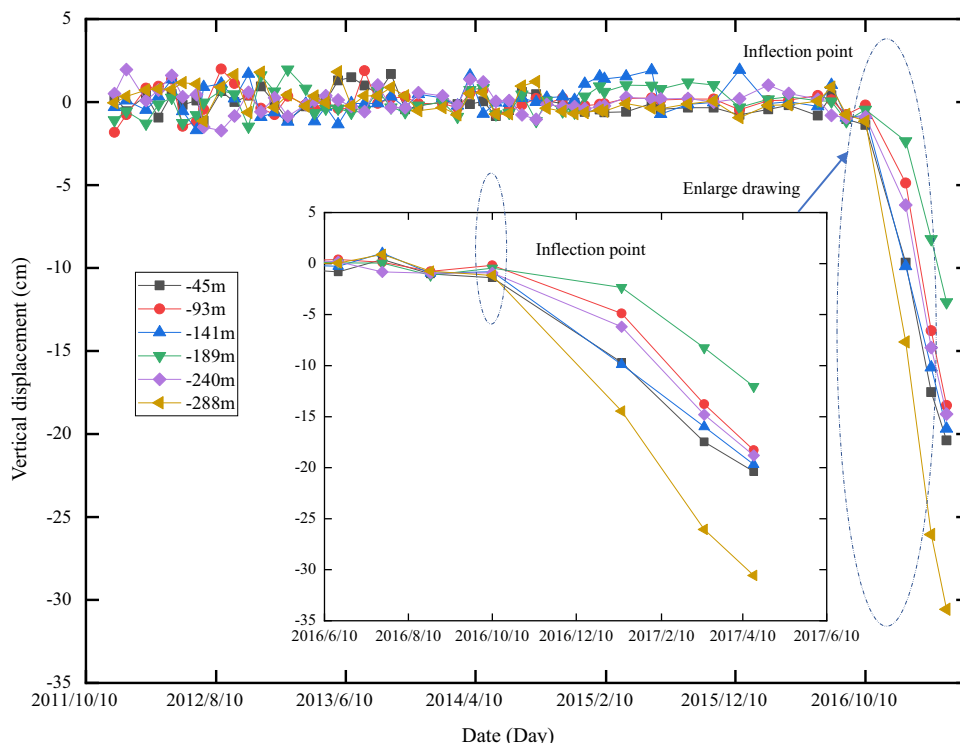
to excavation would therefore cause the horizontal displacement to increase faster than the vertical displacement.

5.3 Deformation Characteristics of the Underground Rock Masses

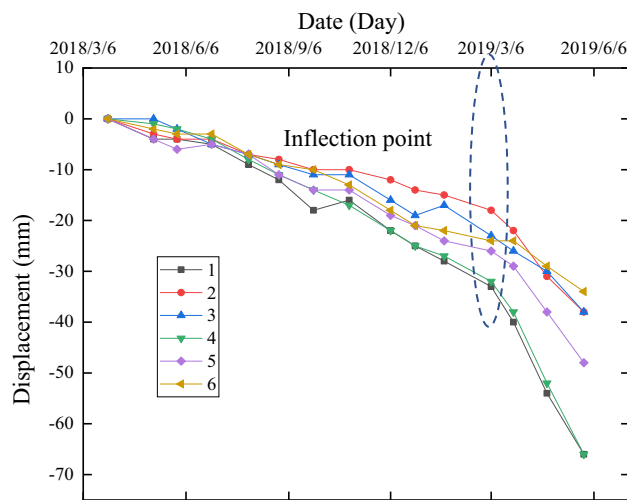
The horizontal displacement of the rock surrounding the drifts and the deformation of the cross sections of the drifts were determined using the data recorded by the multi-point displacement meters and laser convergence meters set up in the − 354 m and − 368 m levels. Figure 3b and c demonstrates the positions of the monitoring points employed.

In the − 354 m sublevel haulage drift, laser convergence meters were set up at points SL3, SL4, and SL6, and a set of multi-point displacement meters were set up at point D2. Convergent behavior was found at all four monitoring points. The curves for SL3 and SL4 appeared to have obvious inflection points, while the data from SL6 were essentially linear.

Fig. 6 Displacements of the monitoring points in the ultra-deep borehole



(a) SL4



(b) SL12

Fig. 7 Displacements measured using the laser converge meters

The largest displacement recorded at SL3 occurred on line 4. Before June 2018, the displacement along each line was small, and the maximum cumulative displacement was less than 3 mm. The displacements along each line began to increase after June 2018 and accelerated again in August. The largest displacement at SL4 occurred on line 2 and the displacement again showed signs of acceleration in June 2018. Monitoring point SL6 was located near fault F3. The displacement–time curves at this point were linear; the largest

displacement occurred along line 1. Figure 7a presents the displacement–time curve of SL4 generated using the data from the convergence meters.

The displacement data recorded at D2 are shown in Fig. 8a. As can be seen, the curves presented indicate that the monitoring points at D2 moved horizontally toward the goaf. The points D2 and SL4 were on the same cross section. The two points closest to the drift (P5 and P6) clearly underwent a period of rapid displacement in 2018 and the movement

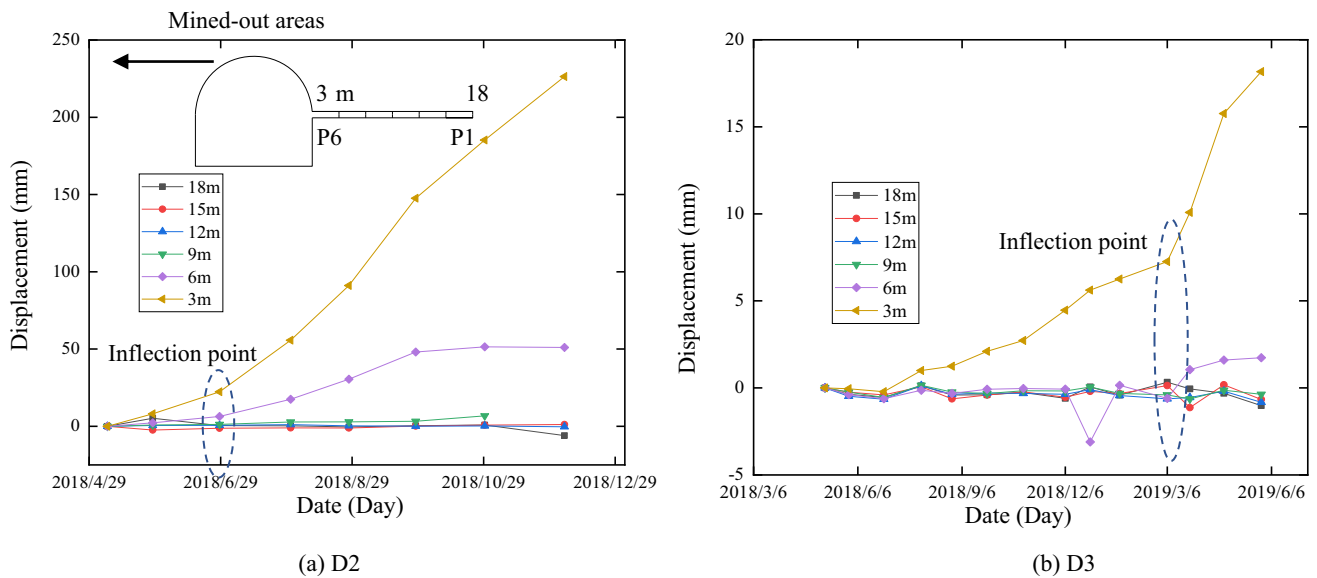


Fig. 8 Displacements measured using the multi-point displacement meters

appeared to have accelerated in June 2018. In October 2018, P4 also showed signs of accelerated displacement, indicating that the horizontal displacement had extended to point P4. By the end of November 2018, the displacement had exceeded its maximum measurement range. The final displacements of P4–P6 in the measuring borehole were 6.8, 51.0, and 226.3 mm, respectively.

In the haulage drift of the – 368 m sublevel, laser convergence meters were set up at SL8, SL10, and SL12 and a set of multi-point displacement meters were set up at D3. The data collected at these points are also plotted in Figs. 7b and 8b. Convergent displacement also occurred at these monitoring points and their displacement–time curves also exhibited obvious points of inflection. D3 could also be seen to be mainly moving horizontally toward the direction of the goaf. The largest displacement at SL8 occurred along line 1, and the overall displacement of the drift cross section was rather symmetrical. The displacement at SL8 was slow to begin with but began to accelerate at the end of March 2019. The displacement at SL10 also began to accelerate at the end of March 2019, and lines 1, 2, and 3 were damaged around this time. Around May 2019, the convergent displacement along line 5 at SL10 exceeded 5 cm.

SL12 was located in a region that was significantly affected by fault F3 (so the surrounding rock is soft and broken). Accelerated displacement also occurred at SL12 in March 2019. The largest displacement occurred along line 1 and was virtually the same as that along line 4. In May 2019, the convergent displacement along line 1 was 66.0 mm. D3 and SL12 were in the same cross section. The displacement of point P6 at D3 began to accelerate around the end of July

2018. In March 2019, the rate of displacement change accelerated again and P5 also began to move more rapidly. As of May 2019, the displacements of points P5 and P6 were equal to 1.7 and 18.2 mm, respectively.

The laser convergence results indicate that the drift mainly underwent convergent displacement. The bottom corner of the drift appeared to undergo the largest displacement and the rock surrounding the drift mainly underwent horizontal displacement. The displacement recorded in the – 354 m level was larger than that in the – 368 m level and the acceleration points in the displacement curves also appeared earlier. The multi-point displacement meter results imply that the closer one was to the goaf, the larger the horizontal displacement of the surrounding rock. Due to the steeply dipping discontinuities that cut through the rock, a downwardly dipping structure was formed to the side of the drift cross section near the mined-out area; an anti-dipping structure was formed on the side that was far from the mined-out area. Due to the horizontal in situ ground stress, buckling failure occurred in the downwardly dipping structure and toppling failure appears in the anti-inclined structure. This also explained why the displacement was large in the bottom corner of the drift.

5.4 Extension of Ground Surface Movement

5.4.1 Determination of the Movement and Break Boundaries

Displacement contours could be drawn using the horizontal GPS displacement data recorded for the monitoring points. These contours obviously change with time as the ground surface moves. Therefore, a series of contour graphs at different

times would be needed to represent the ground movement. To show the displacement data in a single plot, a certain critical displacement should be considered and how the contours formed by these critical displacements change with time needs to be explored. In this work, the critical deformation boundary was chosen to be the deformation corresponding to the most unfavorable value derived using three different criteria based on tilt (i), horizontal strain (ε), and curvature (k). More specifically, movement boundaries were determined using the critical criteria: $i = 3$ mm/m, $\varepsilon = 2$ mm/m, and $k = 0.2 \times 10^{-3}$ /m. Similarly, break boundaries were judged according to the criteria: $i = 10$ mm/m, $\varepsilon = 6$ mm/m, and $k = 0.6 \times 10^{-3}$ /m.

The results of the in situ ground stress tests and monitoring experiments carried out in the Jinshandian Iron Mine indicate that the in situ ground stress is dominated by its horizontal component. As a result, the stress imbalance created when mining was carried out was most significant in the horizontal direction. This caused the horizontal displacement of the continuous deformation zone to increase at a faster rate than the vertical displacement, as shown in Table 4. Therefore, in this paper, the horizontal GPS displacement data were first used to form the displacement field. The horizontal strain was subsequently derived by comparing the horizontal displacement of each monitoring point to the initial distance between the monitoring point and a distant fixed point. The strain values of 0.002 and 0.006 were selected to generate the critical deformation points that are needed to draw movement and break curves.

The movement and break curves thus derived are displayed in Figs. 9a and 10a. Exploratory line 34 was then selected for further analysis. Figures 9b and 10b show the corresponding profiles taken along this exploratory line. As can be seen, the deformation boundaries at different times are connected with the boundaries of the orebodies mined at these times, thus allowing the movement and break angles to be obtained.

5.4.2 Temporal Evolution of the Surface Movement Curves and Angles

According to Fig. 9a, the movement curve moved outwards along a southerly direction by 107 m from April 2008 to January 2012. From January 2012 to December 2016, it moved a further 137 m. From December 2016 to December 2020, it moved a further 265 m. Thus, the extension over the 4-year period from December 2016 to December 2020 was greater than that over the 8-year period from April 2008 to December 2016. This clearly implies that a large-scale surface movement occurred during 2016.

Figure 9b indicates that the movement angles gradually became smaller as the mining level deepened. Furthermore, a sudden change in angle occurred in June 2017. This is

because, after October 2016, due to the failure in the drift, the movement and deformation of the rock mass propagated from deep underground to the ground surface under the effect of the steeply dipping discontinuities. This large-scale surface movement caused a significant reduction in the movement angle — from 66.78° (June 2017) to 60.29° (December 2016).

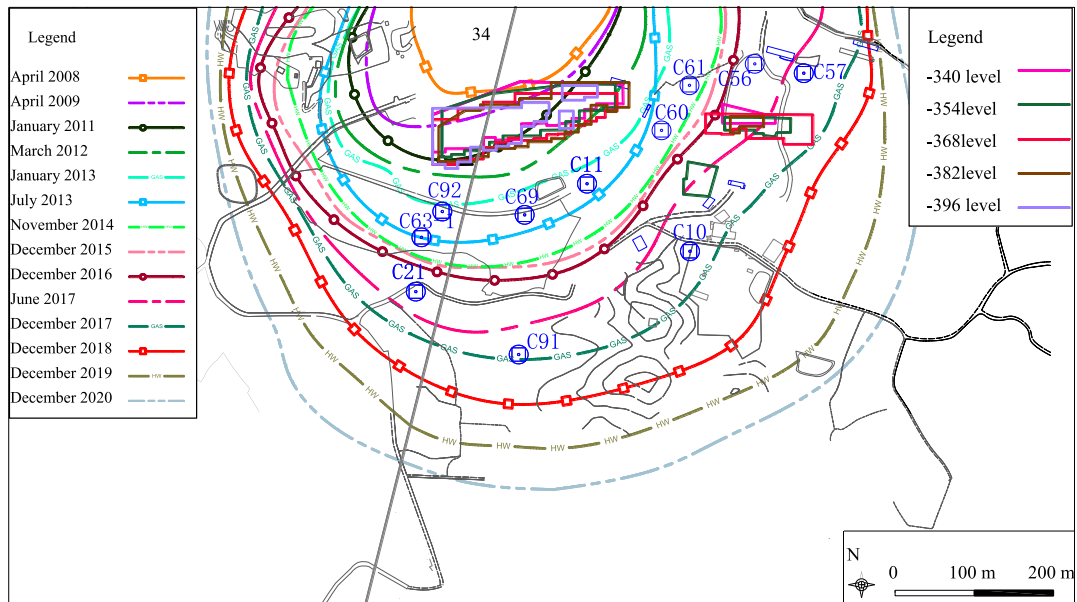
In principle, no buildings and structures should be allowed within the expected range of movement of the ground surface. Therefore, it was important to determine the movement angle as accurately as possible before mining. In the design stage that when the -410 m level in the hanging wall had been completely mined out, the movement angle would be 60° . However, our monitoring results show that, in December 2020, when the -396 m orebody was still being mined (and the -410 m level had not yet been mined out), the movement angle had already reached 48.45° , which was significantly smaller than the expected movement angle. Of course, when the -410 m orebody was eventually mined out, the movement angle would be even smaller (and certainly less than 48.45°). Thus, it is not surprising that a large number of surface buildings and structures already lay in areas that are experiencing ground movement even though they were not expected to.

Li and Xia et al. [17, 38] proposed that the movement angle boundary should be the boundary of broken rock mass rather than the boundary of the mined-out orebody. Between fault F4 and goaf, the rock mass was broken to a significant extent. This method was used to determine the movement angle, the boundary of movement angle was replaced by fault F4 boundary, then the designed movement angle 60° was used to determine the critical point (in terms of movement) on ground surface, which is similar to the principle of the monitoring used herein (Fig. 9b). The new definition of movement angle is suitable for use in the present study.

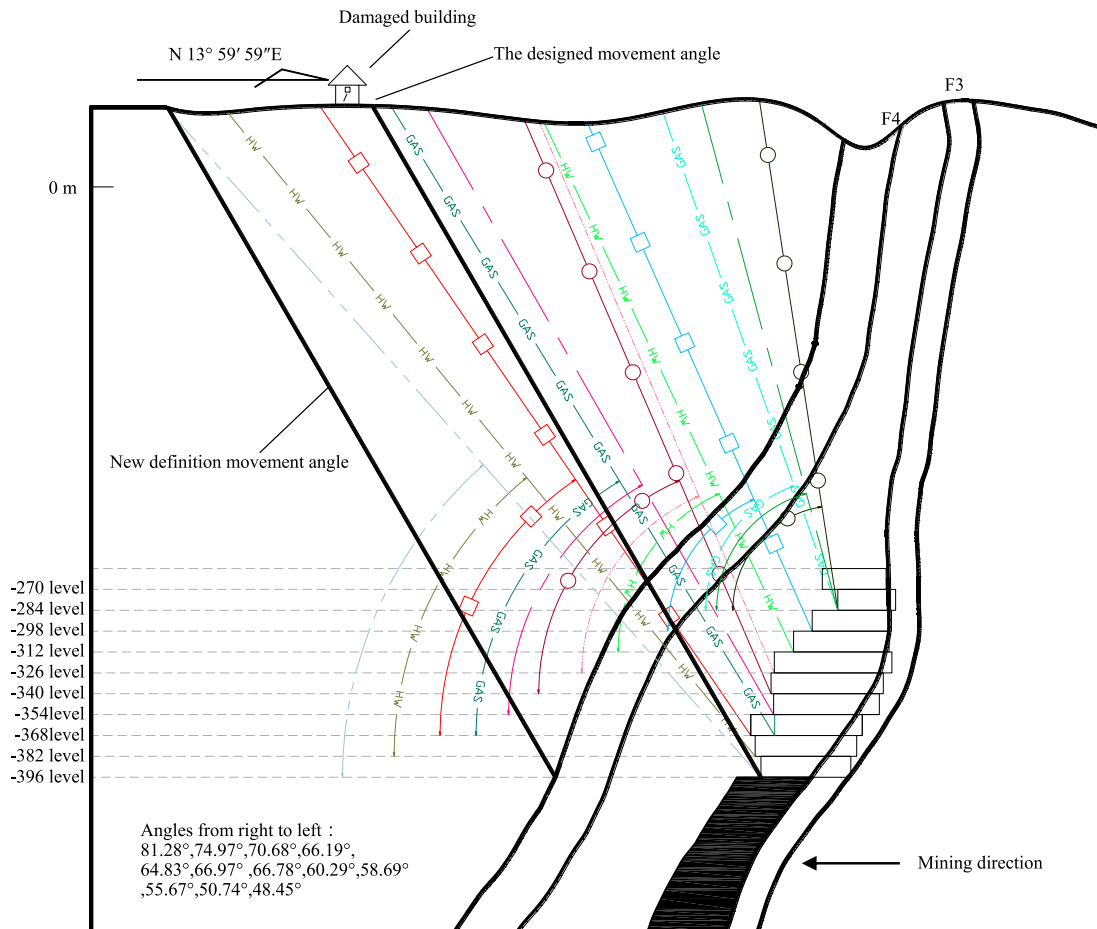
5.4.3 Temporal Evolution of the Surface Break Curves and Angles

Figure 10a shows that the break curve moved outwards along a southerly direction by 47 m from April 2009 to January 2012. From January 2012 to December 2016, it moved a further 104 m. From December 2016 to December 2020, it moved a further 304 m. Thus, the break curve rapidly spread southwards after 2016, causing many cracks to emerge on the ground surface and buildings and structures to suffer serious damage.

Figure 10b illustrates that the break angles also gradually became smaller as the depth of the mining increased. There were sudden changes in break angle in April 2017 and December 2018 which can be related to the mining activity taking place and large-scale subsidence occurring at the surface. Due to the severe deformation of the drift in April 2017,

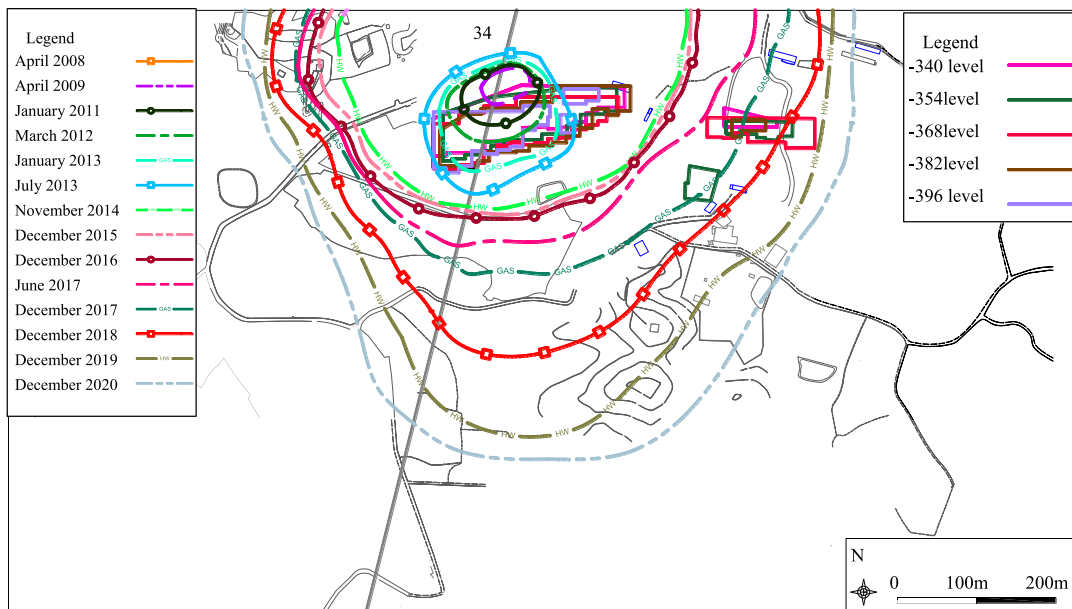


(a) Movement curves (GPS monitoring points in blue).

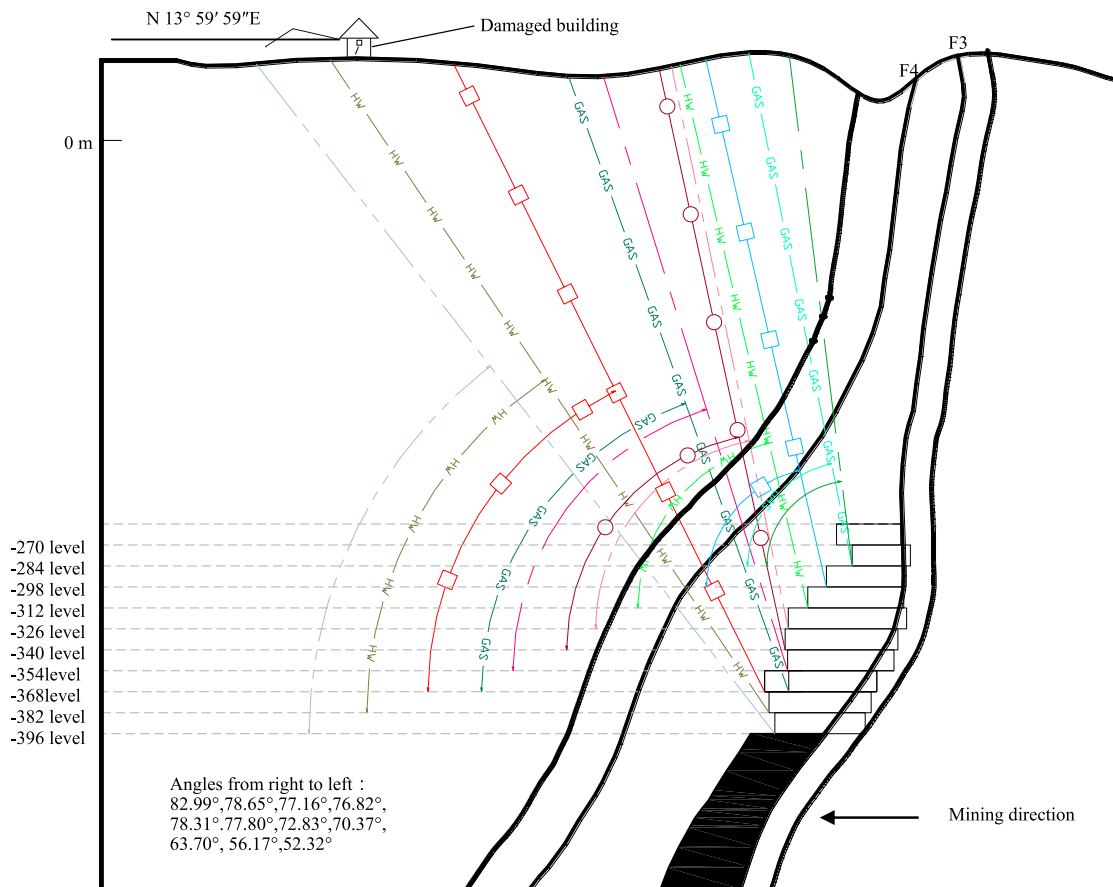


(b) Movement angles along exploratory line 34

Fig. 9 Movement curves and angles



(a) Break curves



(b) Break angles along exploratory line 34

Fig. 10 Break curves and angles

the underground deformation propagated to the surface, significantly increasing the number of cracks at the surface.

The above analysis implies that the movement of the ground surface is closely related to the steeply dipping rock masses present in the mining area. Due to the underground mining activity, fault F3 (which forms one of the orebody's boundaries) slips first. This causes the roof of the goaf to become damaged and fall. The mining activity also triggers the horizontal in situ ground stress in the rock to be released. Coupled with the effect of the slipping fault F3, this causes the anti-dipping rock columns formed to topple. As the mining activity moves to deeper levels, the scope of the damage continues to extend outwards. This disturbance eventually causes fault F4 to slip. This leads to the failure of the haulage drifts in the form of caving and cracking. The movement and break angles become progressively smaller as the mining depth increases. As a result, the actual movement angle (according to the monitoring data) is smaller than the designed movement angle by about 12° .

6 Theoretical Analysis of the Ground Movement Mechanism

6.1 Toppling Failure in Underground Iron Mines

Three-dimensional printed technology was used to study a columnar jointed rock mass [39, 40], and acoustic wave velocity was adopted to improve the Hoek–Brown criterion, which can be better applied in metal mines [41]. Aydan and Kawamoto proposed a cantilever beam model to evaluate the stability of slopes and underground openings in their study [42]. By applying the principle of limit equilibrium to the model, they managed to derive a formula to determine whether or not toppling failure would occur.

In the current context (underground metal mines), the presence of horizontal in situ ground stress and caved rock mass adjacent to the mined-out areas makes the situation very different from the case of a slope with a free surface. According to the field investigations, the dominant disconti-

nities in the hanging wall belong to the first group in Table 1. In this work, exploratory line 36 was selected in order to study the ground movement mechanism. In this case, the height of each sublevel created during underground mining is 14 m.

Ignoring seismic forces, the formula derived by Aydan and Kawamoto [42] can be written in the form

$$P_{i-1} = \frac{P_{i+1}(\eta h_{i+1} - \mu \frac{t_i}{2}) + S_i^w \frac{\bar{h}_i}{2} - \frac{2I_i}{t_i} \left(\frac{\sigma_i}{FS} \pm \frac{N_i^w}{A_i} \right)}{(\eta h_{i-1} + \mu \frac{t_i}{2})} \quad (1)$$

where the positive sign applies to the sidewall, and the negative sign applies to the roof. Equation (1) is used to calculate the stability of the sidewall and roof of an underground opening. If the effects of the horizontal in situ ground stress and caved rock mass are ignored, our calculations suggest that the sidewall will topple if single- or double-level mining can be employed but the roof will not topple.

The situation is more complicated in the current case due to the horizontal in situ ground stress and the fact that the width of the caved rock adjacent to the goaf is unknown (see Fig. 11). It can be assumed that the horizontal in situ ground stress is fully released when the ore is mined and the height of the caved rock is equal to the height of the column adjacent to the goaf. The formula derived by Aydan and Kawamoto was improved based on the above assumptions.

The in situ ground stress produces an overturning moment, whereas the lateral pressure of the caved rock produces an anti-overturning moment. The calculated thickness of the Quaternary overburden layer above the -270 m mining level is 50 m. The rock columns to the side of the mined-out area are in contact with caved rocks (which will have a certain supporting effect) rather than the surface of another rock column. That is, when these rock columns deform, the broken rocks provide lateral support. The horizontal in situ ground stress accelerates the destruction of the sidewall rock columns but delays the failure of the roof because it provides a compressive force between the rock columns.

The condition determining whether or not the rock columns in the roof will topple is thus found to be

$$P_{i-1} = \frac{P_{i+1}(\eta h_{i+1} - \mu \frac{t_i}{2}) + S_i^w \frac{\bar{h}_i}{2} - \frac{2I_i}{t_i} \left(\frac{\sigma_i}{FS} + \frac{N_i^w}{A_i} - \frac{F_{i+1}}{A_i} + \frac{F_{i-1}}{A_i} \right) + \eta Q_{i+1} h_i - \eta Q_{i-1} h_{i-1}}{(\eta h_{i-1} + \mu \frac{t_i}{2})} \quad (2)$$

Calculating the force between the sidewall rock columns that is transferred to the free surface, we also have

$$P_{i-1} = \frac{P_{i+1}(\eta h_{i+1} - \mu \frac{t_i}{2}) + S_i^w \frac{\bar{h}_i}{2} - \frac{2I_i}{t_i} \left(\frac{\sigma_i}{FS} - \frac{N_i^w}{A_i} + \frac{F_{i+1}}{A_i} - \frac{F_{i-1}}{A_i} \right) + \eta Q_{i+1} h_i - \eta Q_{i-1} h_{i-1}}{(\eta h_{i-1} + \mu \frac{t_i}{2})} \quad (3)$$



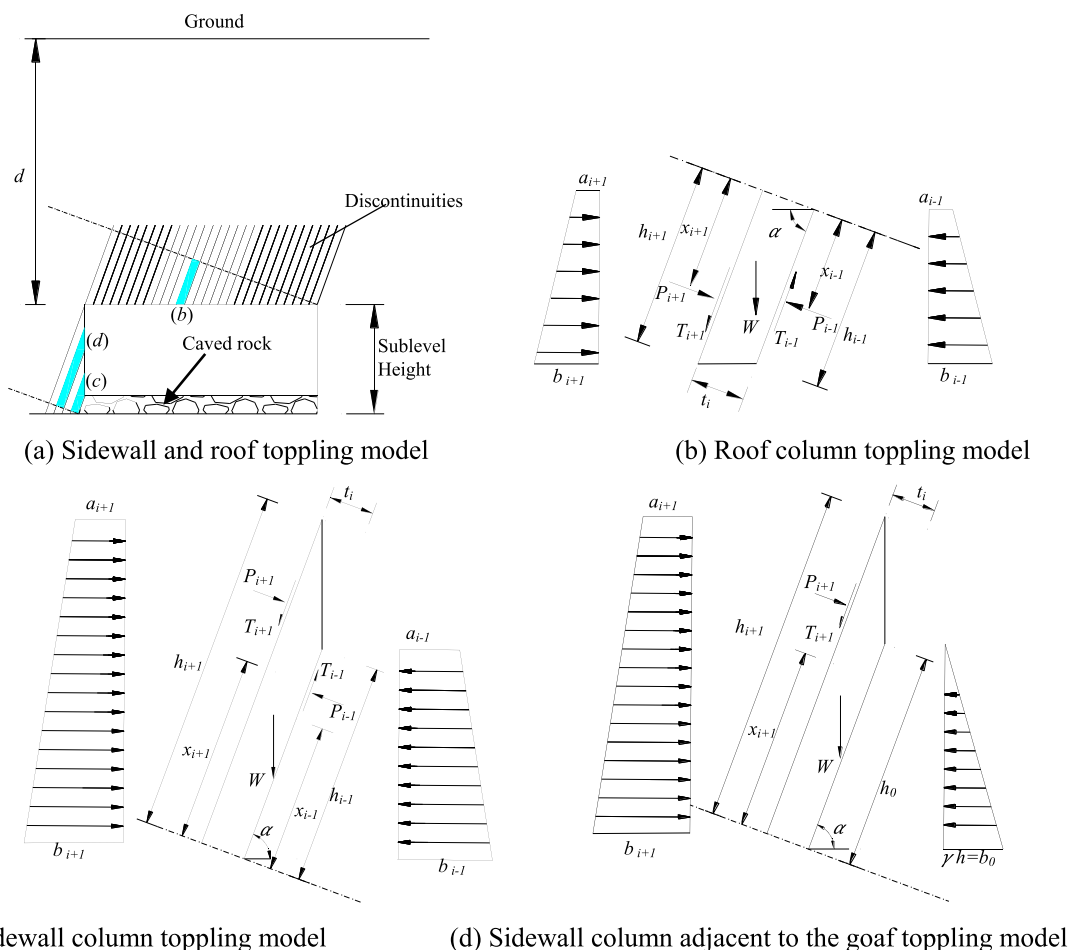


Fig. 11 Cantilever beam model used for the rock masses

The stress acting on the column adjacent to the mined-out area, σ_x (the direction of σ_x is the same as in work by Aydan and Kawamoto [42]), is given by

$$\sigma_x = \frac{F_{i+1} - F_0 - N_i^w}{A_i} + \frac{t_i P_{i+1} (\eta h_{i+1} - \mu \frac{t_i}{2}) + S_i^w \frac{\bar{h}_i}{2} + \eta Q_{i+1} h_{i+1} - \eta Q_0 h_0}{I_i} \tag{4}$$

The value of σ_x is compared with σ_t ; σ_x is greater than σ_t in this work. The rock columns adjacent to the mined-out area will topple.

Note that:

$$\begin{aligned} A_i &= t_i, \quad \bar{h}_i = \frac{1}{2} (h_{i+1} + h_{i-1}), \quad W_i \\ &= \gamma t_i \bar{h}_i, \quad N_i^w = W_i \cos \alpha, \quad S_i^w = W_i \sin \alpha \\ H_i &= \frac{1}{2} (a_i + b_i) h_i \sin \alpha, \quad F_i = H_i \cos \alpha, \quad Q_i \\ &= H_i \sin \alpha, \quad \eta = \frac{2a_i + b_i}{3(a_i + b_i)}, \quad k = \frac{1 - \cos^2 \psi}{1 + \sin^2 \psi} \end{aligned}$$

$$\begin{aligned} a_i &= 1.47\gamma d, \quad b_i = a_i + 1.47\gamma h_i \sin \alpha, \quad a_0 \\ &= 0, \quad b_0 = k\gamma h_0 \sin \alpha \end{aligned}$$

where N represents the normal force, γ is the unit weight of the column, t_i is the thickness of the column, h_i stands for the column height, α is the inclination of the column base, I_i denotes the moment of inertia, FS is the safety factor, η denotes the position of action of the normal force, μ is the friction coefficient of the discontinuity, θ is the friction angle of the discontinuity, ψ is the internal friction angle of caved rock, k is the lateral pressure coefficient, d represents the thickness of the overlying rock above the rock column, σ_t is the tension strength, and H_i is the equivalent horizontal force simplified from the in situ ground stress and lateral stress from the caved rock.

We can obtain the following parameters from Table 1, Ge et al. [37] and Yang [36]:

$$FS = 1, \quad \mu = \tan \theta, \quad \theta = 14.5^\circ, \quad \mu = 0.26, \quad \alpha = 70^\circ, \quad t_i = 0.5 \text{ m}, \quad \gamma = 25.1 \text{ kN/m}^3, \quad \sigma_t = 3 \text{ MPa}, \quad \text{and } \psi = 35^\circ$$

6.2 Fault Slipping Mechanism

Caine et al. and Childs et al. studied fault zone architecture, which consists of a fault core, a damaged zone and protolith [43, 44]. Four types of fault zone were introduced based on the size of the fault core and damaged zone. The fault in the Jinshandian iron mine plays an important role in ground movement which has a small fault core and a large damaged zone. It is necessary to decide when the faults slip and what conditions are required for this to happen. The mechanical model of the fault slip was derived, and the theoretical calculation formula (5) of the fault slip was obtained [45]. Xia et al. [17] used this formula to verify the fault will slide down when $\theta = 65^\circ$, $\lambda = 0.35$, and $\varphi_f = 28^\circ$.

$$\frac{1 - \lambda}{\lambda \tan \theta + \cot \theta} > \tan \varphi_f \quad (5)$$

In (5), λ is the ratio of horizontal (σ_h) and vertical stresses (σ_v), θ and φ_f are the fault dip angle and internal friction angle, γ is the bulk density of the rock around the fault, and h is the burial depth. The above formula does not consider the cohesion c of the faulted rock mass, and the geological investigation indicated that the fault is not cohesionless, so the influence of the cohesion should be considered. Considering cohesion c , Eq. (5) can be written thus:

$$1 - \lambda > \frac{2c}{\sin 2\theta \sigma_v} + (\lambda \tan \theta + \cot \theta) \tan \varphi_f \quad (6)$$

The fault dip angle is 70° , c and φ_f are 0.18 MPa and 26° [37]. Taking $\gamma = 22 \text{ kN/m}^3$, and a burial depth h of 399 m (the average surface elevation is 45 m, the mining level is -354 m), and substituting these into Eq. (6), slip occurs only when the horizontal stress coefficient λ is less than 0.32. It can be concluded that after the horizontal stress is released by 68%, fault F4 begins to slip.

According to the investigation of the damage of the surrounding rock, when the hanging wall was mined to the level of -354 m, the roof of the haulage drift at the -340 m and -410 m stages underwent roof caving, and fault F4 slipped at this time. At the -410 -m level haulage drift, circumferential fractures appeared in the roof where the axis of the 712-transverse drift made a 45° angle with the strike of the fault, vertical fractures appeared on the sidewall which was caused by fault F4 slipping.

6.3 Ground Movement Mechanism

Figure 12 illustrates the important features of the rock masses in the mining area. The hanging wall in the mining area is cut by faults and steeply dipping discontinuities. Anti-dipping rock columns are thus formed which can be modeled as simple cantilever beams. The sublevel haulage drifts are

in relatively broken hornstone, and the haulage drifts are in fault F4 which is unstable.

The fault F3 was subject to disturbance when the orebody was mined because it formed one of the boundaries of the orebody. Slipping therefore occurred which caused the roof to fall under its own weight. The caved rock fell into the mined-out area generating an anti-overturning moment on the rock columns adjacent to the goaf and delaying the destruction of the rock columns. A combination of horizontal in situ ground stress and self-weight stress caused the rock columns to ultimately topple into the goaf.

As the mining activity moves to deeper levels, the number of failing rock columns to the side of the goaf continues to increase. The failure surfaces in adjacent rock columns eventually form a through slip surface. The angle between the slip surface of the surrounding rock and the horizontal is about 60° . After it passes through fault F4, the slipping surface propagates to the ground surface at an angle of about 50° . The drift can be reasonably arranged according to the slipping surface, which greatly reduces the economic loss and ensures safe production in the underground mine. To ensure that the haulage drift does not affect the underground mining operations during their service period, the sublevel haulage drift should be arranged in the area outside the slipping surface, and the level haulage drift should be arranged away from fault F4. Support should be provided for drifts that cannot avoid intersecting faults or slipping surfaces.

Considering the effect of horizontal in situ ground stress, steeply dipping faults and discontinuities, the traditional definition of movement angle will be much smaller than the designed movement angle (about 12°). Therefore, Xia et al. [17] proposed to move the boundary of the movement angle to the fault. In the present work, the boundary of the movement angle was moved to the F4 fault, as shown in Fig. 12, the obtained angle was 62° ; because the orebody at -410 m was not mined, the movement angle exceeds the designed angle of 60° . Using this method, the critical deformation point of the ground movement angle was determined, which can better guide the relocation of the ground surface buildings and avoid underestimating the area subject to movement.

Based on those angles and slipping surface, the goaf surrounding rock mass can be divided into six zones: a caved zone, a failure zone, a toppling-slipping zone, a toppling-deformation zone, a fault-slipping zone, and a movement-deformation zone.

Due to the slippage of fault F3 and the destruction of the roof, a large caved rock mass entered the goaf, and from the roof of the goaf to the ground surface, this formed a continuous collapsed area. Subsequently, the rock surrounding the anti-dip structure on the side of the goaf topples, and the damaged rock column forms a slipping surface (*i.e.*, forming the toppling-slipping zone). A toppling deformation zone is formed between the slipping surface and fault

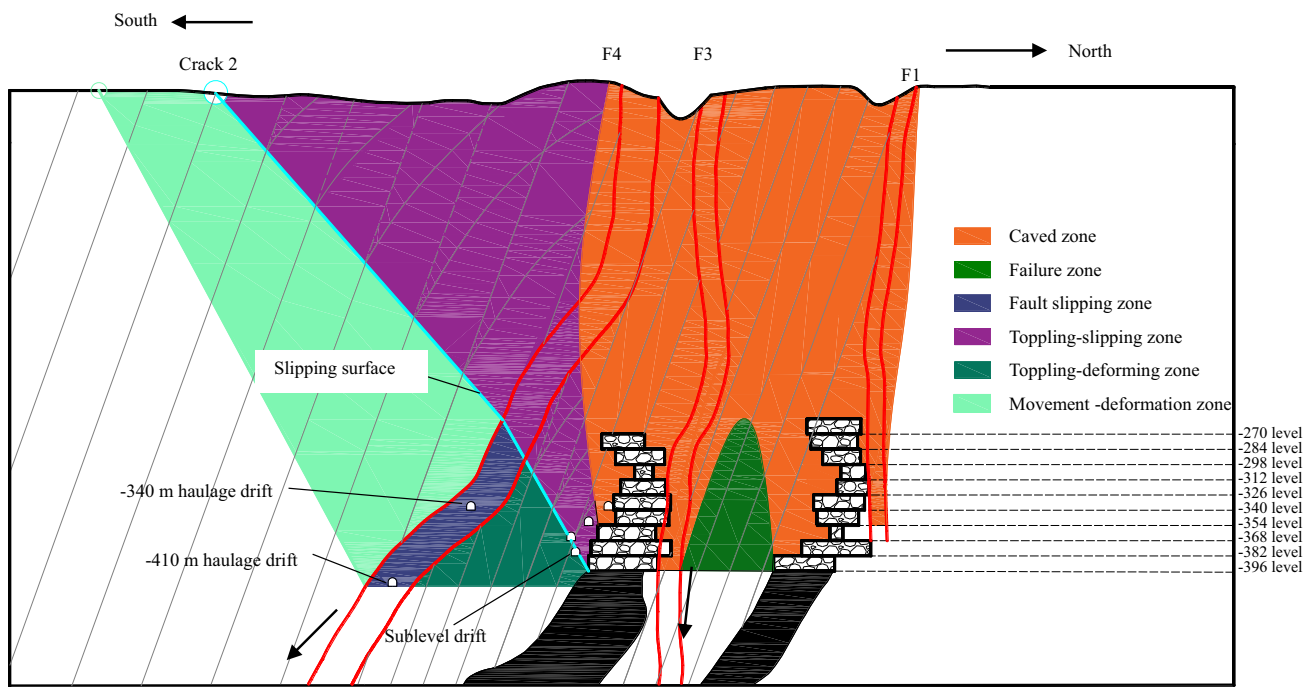


Fig. 12 Ground movement mechanism

F4 as the rock columns are damaged due to toppling. This also has an effect on fault F4 which subsequently slips. The slipping causes the rock masses in the fault to undergo compaction and deformation, resulting in spalling and failure of the roofs and sidewalls of the haulage drifts in the – 340 m and – 410 m levels, the zone is the fault-slipping zone. Above the toppling-slipping zone and fault-slipping zone, the rock mass moves and deforms toward to goaf (the movement-deformation zone). The rock wall between the two orebodies is composed of relatively broken hornstone and quartz diorite. After orebodies I and II have been mined, the rock wall is destroyed, on the whole, forming a failure zone. This increases the severity of the deformation of the surrounding rock in the hanging wall and hence the damage range. Consequently, the damage in the drifts becomes more obvious. The destruction of the rock wall also leads to the formation of an enlarged caved zone with mined-out orebodies I and II that can gradually migrate upwards toward the ground surface. With the deepening of the mining activity, the scope of the damage also migrates downwards while simultaneously expanding away from the mined-out area.

From the above research on ground surface deformation and deformation of the goaf surrounding rock, it can be found that there is a one-by-one correspondence between the two. The roof of the mining area and the surrounding rock near the goaf form a caving area, and the damage to the surrounding rock in the caving area is transmitted to the surface to form a collapse pit. Large tension cracks appear on the surface due to the toppling-slipping failure of the rock mass. As for the

movement-deformation zone, the deformation of goaf surrounding rock mass propagates to the surface within a certain angle at the boundary of fault F4, another boundary of this zone is the critical point for ground movement on the ground surface. The sublevel haulage drift should be arranged in the area outside the slipping surface, and the level haulage drift should be arranged away from fault F4. Buildings and structures should be arranged outside the movement-deformation zone.

The mechanism outlined above explains all the failure phenomena observed in the area (failure of the drifts, the cracking and subsidence at the surface, and the damage incurred by buildings and structures). Firstly, damage and failure sequentially appear in the – 340 m to – 382 m sub-level haulage drifts in the hanging wall. The deformation of the deep rock masses then gradually propagates upwards and reaches the surface after a certain period of time. Major tension cracks (e.g., crack 2 in Fig. 2) are therefore formed on the surface.

7 Discussion

Toppling failure is very common in anti-dip rock slopes, and the theory in this field is mature and widely accepted as accurate; however, in underground metal mines, the damage of the anti-dip structure formed by the cutting of steeply dipping discontinuities is significantly different from that of rock slopes with free surfaces. These differences mainly include

that underground metal mines are generally affected by horizontal in situ ground stress, and the caved rock mass falling from the roof acts on the rock columns on the free surface, which delays the time of toppling and failure of rock columns. However, the degree of stress release of the horizontal in situ ground stress and the height of the caving rock mass are more complicated. Assumptions are adopted here to solve those problems. It is considered that the horizontal in situ ground stress is completely released after the ore body is mined-out, and the height of the caving gravel is equal to that of the rock column on the free face. The main problem here is the degree of release of in situ ground stress, because the lateral pressure of the caving rock mass is small, which can only delay the failure but cannot prevent it. We need to know if toppling failure still occurs when only the self-weight stresses are considered. Lu et al. studied the critical height for rock column toppling failure under self-weight stress, as shown in Eq. (7) [46]:

$$h_{cr} = \frac{t \sin \alpha + \sqrt{t^2 \sin^2 \alpha + 12t \cos \alpha \sigma_t / \gamma}}{6 \cos \alpha} \quad (7)$$

The calculation is conducted when the orebody of -270 m is mined, and the height of the goaf is 14 m. From Eq. (7), the critical height is 7.84 m. This shows that under the action of self-weight stress, the anti-dip rock column will still topple and fail. The effect of horizontal in situ stress will aggravate the rate of rock column failure and the range of ground movement.

Numerical simulation can be performed to evaluate the degree of release of horizontal in situ ground stress and the interaction between the caving rock mass and rock columns on the free surface. Whether the release degree of the horizontal in situ ground stress and the height of the caved rock mass at the free surface will change the failure mechanism of the rock column requires further research.

8 Conclusion

(1) The strikes of the surface cracks were essentially the same as those of the main discontinuities in the rock mass, i.e., they formed due to tensile failure along discontinuities that were weak. Faults F3 and F4 were the main reason for the emergence of collapse pits IV and VI. After October 2016, the displacement increased sharply, which was caused by the slipping of fault F4. The ratio of the horizontal to vertical displacement was greater than 1 (caused by the release of horizontal in situ ground stress), the deformation and damage caused by the underground mining activity gradually propagated from deep underground to the surface.

- (2) The steeply dipping discontinuities played a key role in drift failure. The sublevel haulage drift failure caused by the toppling failure of the anti-dip rock column, and the level haulage drift failure induced by slipping of fault F4. As the size of the failing rock column increased, a slipping surface at about 60° to the horizontal emerged near the surrounding rock of the goaf, which was confirmed in the drift failure site investigation and the microseismic fracture event signal.
- (3) The movement and break angles decreased as the mining depth increased. The actual monitored movement angle was also less than the expected movement angle by about 12°; the movement angle should be determined by the new definition proposed by Xia et al. [17], which was applicable in this case.
- (4) The toppling failure mechanism was proposed in the underground iron mine with consideration of horizontal in situ ground stress and the extent of the caved rock mass. The fault slipping mechanism can provide a reasonable illustration of the level haulage drift failure. First, fault F3 started to slip due to the disturbance caused by the mining activity. Then, the horizontal in situ ground stress caused the rock columns to topple toward the mined-out area. The damaged rock columns formed a through slipping surface at 60° to the horizontal. Fault F4 was subsequently disturbed by movement and deformation of the nearby rock and then slipped itself. The rock columns above the fault subsequently toppled, forming a slipping surface at 50° to the horizontal. This then propagated all the way to the surface which caused a tension crack to appear on the ground surface.
- (5) There are six zones around the goaf rock mass: a caved zone, a failure zone, a toppling-slipping zone, a toppling-deformation zone, a fault-slipping zone, and a movement-deformation zone. The sublevel haulage drift should be arranged in the area outside the slipping surface, and the level haulage drift should be arranged away from fault. Buildings and structures should be arranged outside the movement-deformation zone.

Author contributions TW was involved in conceptualization, methodology, investigation, writing—original draft, writing—review and editing. CC contributed to supervision, conceptualization, resources, project administration. KX was involved in conceptualization, investigation, methodology, writing—review and editing. YS contributed to investigation, methodology. XL and KY were involved in investigation.

Funding Financial support for this work was provided by the Young Scholar Fund of National Natural Science Foundation of China (grant no. 42002292). We are very grateful for the Foundation's continuous support.

Declarations

Conflict of interest The authors declare that they have no competing interests.

References

- Lupo, J.F.: Evaluation of deformations resulting from mass mining of an inclined orebody. Colorado School of Mines (1996)
- Villegas, T.; Nordlund, E. (2008a) Numerical analysis of the hangingwall failure at the Kiirunavaara mine. In: Proceedings of MassMin 2008, the 5th international conference and exhibition on mass mining, Lulea University of Technology, Lulea, Sweden, pp 867–876.
- Villegas, T.; Nordlund, E. (2008b) Numerical simulation of the hangingwall subsidence using PFC2D. In: Proceedings of MassMin 2008, the 5th international conference and exhibition on mass mining, Lulea University of Technology, Lulea, Sweden, pp 907–916.
- Villegas, T.; Nordlund, E.: Time-dependent movements of the hangingwall at the Kiirunavaara Mine Int. J. Min. Reclam. Environ. **26**(2), 119–133 (2012)
- Svartsjaern, M.; Saiang, D.: Discrete element modelling of footwall rock mass damage induced by sub-level caving at the Kiirunavaara mine. Minerals **7**, 109 (2017)
- Svartsjaern, M.: A prognosis methodology for underground infrastructure damage in sublevel cave mining. Rock Mech. Rock Eng. **52**, 247–263 (2019)
- Xia, K.Z.; Chen, C.X.; Fu, H.; Pan, Y.C.; Deng, Y.Y.: Mining-induced ground deformation in in-situ ground stress metal mines: a case study. Eng. Geol. **210**, 212–230 (2016)
- Xia, K.Z.; Chen, C.X.; Zheng, Y.; Zhang, H.N.; Liu, X.M.; Deng, Y.Y.; Yang, K.Y.: Engineering geology and ground collapse mechanism in the Chengchao iron-ore mine in China. Eng. Geol. **249**, 129–147 (2019)
- Deng, Y.Y.; Chen, C.X.; Xia, K.Z.; Pang, H.S.; Sun, C.Y.; Yang, K.Y.; Zheng, X.W.: Investigation on the distribution characteristics of ground cracks in the Chengchao Iron Mine China. Environ. Earth Sci. **78**, 280 (2019)
- Deng, Y.Y.; Chen, C.X.; Xia, K.Z.; Sun, C.Y.; Zheng, X.W.: A field investigation on the distribution characteristics of structure cracks in the Chengchao Iron Mine, China. Arab. J. Geosci. **13**, 231 (2020)
- Cheng, G.W.; Chen, C.X.; Li, L.C.; Zhu, W.C.; Yang, T.H.; Dai, F.; Ren, B.: Numerical modelling of strata movement at footwall induced by underground mining. Int. J. Rock Mech. Min. Sci. **108**, 142–156 (2018)
- Li, X.S.; Li, Q.H.; Hu, Y.J.; Teng, L.; Yang, S.: Evolution characteristics of mining fissures in overlying strata of stope after converting from open-pit to underground. Arab. J. Geosci. **14**(24), 1–18 (2021)
- Lu, R.; Ma, F.S.; Guo, J.; Zhao, H.J.: Analysis and monitoring of roadway deformation mechanisms in nickel mine, China. Concurr. Comput. Pract. Exp. **2018**, e4832 (2018)
- Ma, F.S.; Zhao, H.J.; Zhang, Y.M.; Guo, J.; Wei, A.H.; Wu, Z.Q.; Zhang, Y.L.: GPS monitoring and analysis of ground movement and deformation induced by transition from open-pit to underground mining. J. Rock Mech. Geotech. Eng. **4**(1), 82–87 (2012)
- Xia, K.Z.; Chen, C.X.; Deng, Y.Y.; Xiao, G.F.; Zheng, Y.; Liu, X.M.; Fu, H.; Song, X.G.; Chen, L.L.: In situ monitoring and analysis of the mining-induced deep ground movement in a metal mine. Int. J. Rock Mech. Min. Sci. **109**, 32–51 (2018)
- Xia, K.Z.; Chen, C.X.; Lu, Z.D.; Yang, K.Y.; Zheng, Y.; Pan, H.S.; Sun, C.Y.: Investigation of the ground movement due to underground mining at the Jinshandian Iron Mine in China. Environ. Earth Sci. **78**, 715 (2019)
- Xia, K.Z.; Chen, C.X.; Wang, T.L.; Yang, K.Y.; Zhang, C.Q.: Investigation of mining-induced fault reactivation associated with sublevel caving in metal mines. Rock Mech. Rock Eng. **55**, 5953 (2022)
- Wang, F.; Jiang, B.; Chen, S.; Ren, M.: Surface collapse control under thick unconsolidated layers by backfilling strip mining in coal mines. Int. J. Rock Mech. Min. Sci. **113**, 268–277 (2019)
- Chen, T.; Mitri, H.S.: Strategic sill pillar design for reduced hanging wall overbreak in longhole mining. Int. J. Min. Sci. Technol. **31**, 975–982 (2021)
- Wempen, J.M.: Application of DInSAR for short period monitoring of initial subsidence due to longwall mining in the mountain west United States. Int. J. Min. Sci. Technol. **30**, 33–37 (2020)
- Malinowska, A.; Hejmanowski, R.; Dai, H.Y.: Ground movements modeling applying adjusted influence function. Int. J. Min. Sci. Technol. **30**, 243–249 (2020)
- Aydan, O.; Akagi, T.; Kawamoto, T.: The squeezing potential of rocks around tunnels: theory and prediction. Rock Mech. Rock Eng. **26**, 137–163 (1993)
- Shen, B.; Barton, N.: The disturbed zone around tunnels in jointed rock masses. Int. J. Rock Mech. Min. Sci. **34**(1), 117–125 (1997)
- Gao, F.Q.; Stead, D.; Kang, H.P.: Numerical simulation of squeezing failure in a coal mine roadway due to mining-induced stresses. Rock Mech. Rock Eng. **48**, 1635–1645 (2015)
- Bai, Q.S.; Tu, S.H.; Zhang, C.; Zhu, D.F.: Discrete element modeling of progressive failure in a wide coal roadway from water-rich roofs. Int. J. Coal Geol. **167**, 215–229 (2016)
- Jing, H.W.; Wu, J.Y.; Yin, Q.; Wang, K.: Deformation and failure characteristics of anchorage structure of surrounding rock in deep roadway. Int. J. Min. Sci. Technol. **30**, 593–604 (2020)
- Sun, X.M.; Zhao, C.W.; Zhang, Y.; Chen, F.; Zhang, S.K.; Zhang, K.Y.: Physical model test and numerical simulation on the failure mechanism of the roadway in layered soft rocks. Int. J. Min. Sci. Technol. **31**, 291–302 (2021)
- Ding, K.; Ma, F.S.; Guo, J.; Zhao, H.J.; Lu, R.; Liu, F.: Investigation of the mechanism of roof caving in the Jinchuan nickel mine, China. Rock Mech. Rock Eng. **51**, 1215–1226 (2018)
- Tan, W.H.; Kulatilake, P.H.S.W.; Sun, H.B.; Sun, Z.H.: Effect of faults on in-situ stress state in an open-pit mine. Electron. J. Geotech. Eng. **19**, 9597–9629 (2014)
- Tan, W.H.; Kulatilake, P.H.S.W.; Sun, H.B.: Influence of an inclined rock stratum on in-situ stress state in an open-pit mine. Geotech. Geol. Eng. **32**(1), 31–42 (2014)
- Hao, Y.H.; Azzam, R.: The plastic zones and displacements around underground openings in rock masses containing a fault. Tunn. Undergr. Sp. Technol. **20**(1), 49–61 (2005)
- Zhao, Z.L.; Jing, H.W.; Zhang, L.; Shi, X.S.: Physical modeling investigation on deformation characteristic and roof instability mechanism of deep rectangular roadway in layered rock mass. Arab. J. Geosci. **15**, 58 (2022)
- Shen, B.; King, A.; Guo, H.: Displacement, stress and seismicity in roadways roofs during mining-induced failure. Int. J. Rock Mech. Min. Sci. **44**, 672–688 (2008)
- Xin, W.; Kulatilake, P.H.S.W.; Song, W.D.: Stability investigations around a mine tunnel through three-dimensional discontinuum and continuum stress analyses. Tunn. Undergr. Sp. Technol. **32**(32), 98–112 (2012)



35. Li, A.; Xu, N.W.; Dai, F.; Gu, G.K.; Hu, Z.H.; Liu, Y.: Stability analysis and failure mechanism of the steeply inclined bedded rock masses surrounding a large underground opening. *Tunn. Undergr. Sp. Technol.* **77**, 45–58 (2018)
36. Yang, K.Y.: Study on ground pressure activity law of a metal mine adopted non-pillar sublevel caving method. Institute of Rock and Soil Mechanics Chinese Academy of Sciences, Wuhan (2019).
37. Ge, X.R.; Bai, S.W.; Chen, C.X., et al.: Research on surface deformation problems and control strategies of underground mining in east area of Jinshandian iron mine. Institute of Rock and Soil Mechanics, Chinese Academy of Sciences, Wuhan (1999).
38. Li, C.L.: Study on mechanism and prediction of ground subsidence in mines using caving technique. University of Science and Technology Beijing, Beijing (2007).
39. Xia, Y.J.; Liu, B.C.; Zhang, C.Q.; Liu, N.; Zhou, H.; Chen, J.; Tang, C.A.; Gao, Y.; Zhao, D.C.; Meng, Q.K.: Investigations of mechanical and failure properties of 3D printed columnar jointed rock mass under true triaxial compression with one free face. *Geomech. Geophys. Geo* **8**, 26 (2022)
40. Xia, Y.J.; Zhang, C.Q.; Zhou, H.; Hou, J.; Su, G.S.; Gao, Y.; Liu, N.; Singh, H.K.: Mechanical behavior of structurally reconstructed irregular columnar jointed rock mass using 3D printing. *Eng. Geol.* **268**, 105509 (2020)
41. Xia, K.Z.; Chen, C.X.; Wang, T.L.; Zheng, Y.; Wang, Y.: Estimating the geological strength index and disturbance factor in the Hoek-Brown criterion using the acoustic wave velocity in the rock mass. *Eng. Geol.* **306**, 106745 (2022)
42. Aydan, O.; Kawamoto, T.: The stability of slopes and underground openings against flexural toppling and their stabilization. *Rock Mech. Rock Eng.* **25**(3), 143–165 (1992)
43. Caine, J.S.; Evans, J.P.; Forster, C.B.: Fault zone architecture and permeability structure. *Geology* **24**(11), 1025–1028 (1996)
44. Childs, C.; Manzocchi, T.; Walsh, J.J.; Bonson, C.G.; Nicol, A.; Schopfer, M.P.J.: A geometric model of fault zone and fault rock thickness variations. *J. Struct. Geol.* **31**, 117–127 (2009)
45. Li, Z.L.; Dou, L.M.; Cai, W.; He, J.; Wang, G.F.; Liu, J.; Han, R.J.: Fault-pillar induced rock burst mechanism of thick coal seam in deep mining. *Chin. J. Rock Mech. Eng.* **32**(2), 333–342 (2013) **(in Chinese)**
46. Lu, H.F.; Liu, Q.S.; Chen, C.X.: Improvement of cantilever beam limit equilibrium model of counter-tilt rock slopes. *Rock Soil Mech.* **33**(2), 577–584 (2012) **(in Chinese)**

Springer Nature or its licensor (e.g. a society or other partner) holds exclusive rights to this article under a publishing agreement with the author(s) or other rightsholder(s); author self-archiving of the accepted manuscript version of this article is solely governed by the terms of such publishing agreement and applicable law.

